

Characterization of the Shock Wave Structure in Water

Emilie Teitz
Marquette University

Recommended Citation

Teitz, Emilie, "Characterization of the Shock Wave Structure in Water" (2017). *Master's Theses (2009 -)*. 401.
http://epublications.marquette.edu/theses_open/401

Characterization of the Shock Wave Structure in Water

By

Emilie Maria Teitz, B.S.

A Thesis submitted to the Faculty of the Graduate School,
Marquette University, in Partial Fulfillment of the Requirements for
The Degree of Master of Science

Milwaukee, Wisconsin

May 2017

ABSTRACT

CHARACTERIZATION OF THE SHOCK WAVE STRUCTURE IN WATER

Emilie Maria Teitz, B.S.

Marquette University, 2017

The scientific community is interested in furthering the understanding of shock wave structures in water, given its implications in a wide range of applications; from researching how shock waves penetrate unwanted body tissues to studying how humans respond to blast waves. Shock wave research on water has existed for over five decades. Previous studies have investigated the shock response of water at pressures ranging from 1 to 70 GPa using flyer plate experiments. This report differs from previously published experiments in that the water was loaded to shock pressures ranging from 0.36 to 0.70 GPa. The experiment also utilized tap water rather than distilled water as the test sample.

Flyer plate experiments were conducted in the Shock Physics Laboratory at Marquette University to determine the structure of shock waves within water. A 12.7 mm bore gas gun fired a projectile made of copper, PMMA, or aluminum at a stationary target filled with tap water. Graphite break pins in a circuit determined the initial projectile velocity prior to coming into contact with the target. A Piezoelectric timing pin (PZT pin) at the front surface of the water sample determined the arrival of the leading wave and a Photon Doppler Velocimeter (PDV) measured particle velocity from the rear surface of the water sample. The experimental results were compared to simulated data from a Eulerian Hydrocode called CTH [1]. The experimental results differed from the simulated results with deviations believed to be from experimental equipment malfunctions. The main hypothesis being that the PZT pin false triggered, resulting in measured lower than expected shock velocities. The simulated results were compared to published data from various authors and was within range.

ACKNOWLEDGMENTS

Emilie Maria Teitz, B.S.

Obtaining a Masters of Science in Mechanical Engineering in just two semesters is not a solo pursuit, and so I would like to express my deepest appreciation to:

My advisor Dr. John P. Borg, for believing in my abilities, educating me, and giving me a future.

My Dad, words cannot express my entire gratitude but to start, thank you for teaching me the value of hard work, how to accomplish any goal, and helping me become the best version of myself.

My Mom and Sister, for their constant love and support, and for teaching me the value of compassion.

My mentor, Lindsay Shifley, for teaching me the power of leaning in.

My amazing friend, John Luepke, for being my support system and study buddy for five years.

To the girls of the third floor Xi House, for teaching me how to love life and how to realize my potential.

My woodshop teacher, Mr. Gerlach, for encouraging me to go to engineering school when I did not think it was possible.

My fifth-grade teacher, Mrs. Rogers, for being the first teacher who saw potential in me and for putting me on the path I am today.

My close friends, for all of the laughs and encouragements through the late nights in Engineering Hall.

To the Marquette Triathlon Team, for helping me find my passion for cycling and running and giving me a relaxing outlet on campus.

And last, but definitely not least, the Marquette University administration and faculty.

TABLE OF CONTENTS

ACKNOWLEDGMENTS	i
LIST OF FIGURES	iv
1. Introduction	1
2. Background.....	3
2.1 Literature Review.....	3
3. Theory.....	13
3.1 Water: A Brief Overview	13
3.2 Shock Wave Overview.....	22
3.3 The Hugoniot Equations.....	28
3.4 The Hugoniot Planes	29
3.5 Shock Velocity	32
3.6 Impedence Matching.....	32
3.7 Assignment of a Hugoniot	37
4. Methodology.....	40
4.1 Instrumentation Design	40
4.2 Projectile Design	43
4.3 Target Design	45
4.4 Sputter Coating.....	49
4.4 Target Design Validation	52
4.5 Target Assembly Process	56
5. Diagnostics	60
5.1 Pressure Measurement Design	60
5.2 Velocity Pins	62

5.3 Piezoelectric Pin.....	63
5.4 Photon Doppler Velocimeter.....	66
5.5 Data Analysis	68
6. Results and Discussion	80
6.1 Comparison to Simulations	85
6.2 Comparison to Published Data.....	96
6.3 Analysis.....	99
7. Conclusion	101
7.1 Future work	101
7.2 Conclusions	102
BIBLIOGRAPHY.....	105
8. Appedix.....	108

LIST OF FIGURES

Figure 1: Experimental image used to determine shock velocity [13].	8
Figure 2: Demonstration of the experimental analysis for Mori et. al [2].	9
Figure 3: Experimental set up [14].	10
Figure 4: Experimental image used to determine the shock velocity by Nagayama [14].	10
Figure 5: Lynse experimental setup [15].	11
Figure 6: Experimental results depicting a kink in the data [16].	12
Figure 7: A schematic of a water molecule in the liquid state.	14
Figure 8: Tetrahedral molecular form of ice [18]	15
Figure 9: Pressure (GPA) versus temperature (k) of the ice forms [18]	16
Figure 10: Density versus temperature for water in the solid line [18]	18
Figure 11: Isothermal compressibility, X_T , versus temperature, t [10].	19
Figure 12: Viscosity versus pressure of liquid water at three fixed temperatures [10]. ..	20
Figure 13: Diffusivity versus pressure for liquid water [10]	21
Figure 14: Typical stress versus strain graph.	22
Figure 15: Typical stress versus strain graph with the three zones labeled.	24
Figure 16: Demonstration of the travel times of the shock and particle velocity.	26
Figure 17: Demonstration of a left and right going wave in pressure-particle velocity space.	27
Figure 18: Schematic showing the flyer, A, and target, B, C, and D.	33
Figure 19: Left and right going waves in the pressure-particle velocity space for target pieces A and B.	35
Figure 20: Left and right going waves in the pressure-particle velocity space for target pieces B and C.	37
Figure 21: Graphical demonstration of a Hugoniot line in U_s - U_p space	38
Figure 22: Demonstration of the Curve Fitting Application in MATLAB's output.	39
Figure 23: Haskel Gas Booster	41
Figure 24: Stripper box, velocity break pins, and projectile	42
Figure 25: Overview picture of the equipment on the small gas gun	42
Figure 26: CAD drawing of the sabot design with all dimensions in inches.	43

Figure 27: The projectile flyer made from copper, aluminum, or PMMA. Here all dimensions are in inches.	44
Figure 28: Physical flyers made from (left to right) PMMA, aluminum, and copper	45
Figure 29: Nylon sabots with two O-Rings and flyers inserted.....	45
Figure 30: Target mounted to the target plate.....	46
Figure 31: Target components laid out	47
Figure 32: MTI Corporation model GSL-1100X-SPC12-LD sputter coating machine located in Marquette University Dental Research Laboratory	49
Figure 33: Graph for determining thickness of the gold sputter coating [18].	51
Figure 34: A sample after being sputter coated for two minutes.....	51
Figure 35: Hydrocode set up.....	52
Figure 36: Pressure wave propagating at $5.28e-8$ seconds	53
Figure 37: Pressure wave propagating at $1.01e-7$ seconds	53
Figure 38: Pressure wave propagating at $1.51e-7$ seconds	53
Figure 39: Pressure wave propagating at $2.50e-7$ seconds	53
Figure 40: Pressure wave propagating at $5.52e-7$ seconds	54
Figure 41: Pressure wave propagating at $4.51e-7$ seconds	54
Figure 42: Pressure wave propagating at $5.50e-7$ seconds	54
Figure 43: Pressure wave propagating at $6.52e-7$ seconds	54
Figure 44: Pressure wave propagating at $7.51e-7$ seconds	55
Figure 45: Pressure wave propagating at $8.51e-7$ seconds	55
Figure 46: Pressure wave propagating at $9.02e-7$ seconds	55
Figure 47: Pressure wave propagating at $1.00e-6$ seconds	55
Figure 48: Pressure wave propagating at $1.10e-6$ seconds	56
Figure 49: Pressure wave propagating at $1.20e-6$ seconds	56
Figure 50: Dwyer DPMA-401 LCD screen with a pressure control valve.....	61
Figure 51: Swagelok gage and Dwyer pressure transducer	62
Figure 52: Agilent Technologies DOS-X-3034A oscilloscope with an output from velocity break pins	63
Figure 53: Piezoelectric Pin [19]	64
Figure 54: Soldering set up for connecting a BNC cable to a PZT pin.	65

Figure 55: BNC cable aligned to a PZT pin.	65
Figure 56: Schematic of the Photon Doppler velocimeter (PDV) at Marquette University.	67
Figure 57: Time versus Voltage output from the break pin oscilloscope	69
Figure 58: Time versus Amplitude graph of the complete set of data.....	70
Figure 59: Time versus Amplitude graph with an FFT performed in the early section of the data.	71
Figure 60: Time versus Amplitude graph with a zoomed in portion of the FFT window.	72
Figure 61: Frequency versus Amplitude for a single FFT sample window.....	73
Figure 62: Time versus Amplitude of the frequency data with an FFT performed.	74
Figure 63: Contour plot of time versus frequency	75
Figure 64: Particle Velocity versus Pressure for the flyer and driver interface.....	76
Figure 65: Particle Velocity versus Pressure for the driver and water interface.	77
Figure 66: Experimental Results of the small gas gun experiment conducted at Marquette University.....	83
Figure 67: Experimental Results of the small gas gun experiment conducted at Marquette University presented with uncertainty analysis.	85

Figure 68: Simulated results used to find the wave traveling time.....	86
Figure 69: Experimental and simulated results.....	88
Figure 70: Experimental and simulated results displayed with error bars.....	89
Figure 71: PZT pin oscilloscope output.....	92
Figure 72: Simulated Results without a PZT pin in the design.	93
Figure 73: Simulated Results with a PZT pin in the design.	93
Figure 74: Experimental Results of the small gas gun experiment conducted at Marquette University compared to published data.....	96
Figure 75: Original target sample with two PDV collimators exiting the design mounted onto the target plate.....	108
Figure 76: Modified target design for shot one.	109
Figure 77: Target for the second shot featuring one collimator and one PZT pin.....	110

1. Introduction

The scientific community is interested in furthering the understanding of shock wave structure of water, given its implications in a wide range of applications; from researching how shock waves penetrate unwanted body tissues to studying how humans respond to blast effects. Shock waves research steamed from early percussion research but got its bearings in the early 19th century with scientists like Poisson and Newton [1]. Shock wave research on water specifically dates back to a little over five decades ago [2]. There is interest in the health field, defense industry, and planetary sciences to understand the effects of shocking water.

Shock waves have even been used to purify water containing copper, boron, and lead [3]. The study of shock waves in water is important as the properties of water are close to that of living tissues which helps in the medical and defense industry [2]. There exist opportunities to experimentally characterize the shock effects of water at low pressures as the current published data below 2 GPa has large variations in the results according to Nagayama [4].

An experiment was conducted at Marquette University to characterize the shock wave structure of water below 2 GPa. The study utilized a 12.7 mm light gas gun which fired a projectile into a water sample. The projectile ranged in velocities from 200 to 350 m/s. This report differs from previously published experiments in that the water was loaded to shock pressures ranging from 0.36 to 0.70 GPa. The experiment also utilized tap water rather than distilled water as the test sample.

The experimental results are compared to simulated results from a Eulerian Hydrocode named CTH developed by Sandia National Laboratories and compared to published data from various authors [5].

2. Background

2.1 Literature Review

In the early 19th century, little was known about shock waves. The public recognized a shock wave as an earth quake on land or in the sea. In 1808, Poisson described a shock wave as “intense sound” where the “molecule velocities can no longer be regarded as very small.” Stokes used the words “surface of discontinuity” to describe a shock wave in 1848. Euler started making headway by studying the amplitude of waves in his work. Early research by physicists, chemists, and explosives engineers along with the many wars in history changed the usage of the term “shock”. In 1929, Meyers *Konversationslexihom*, a German encyclopedia used the term ‘shock wave’ to describe a shock wave as one knows the term today for the first time [1].

The study of shock waves as one knows them today, started with percussion research. Percussion research began by studying small scale items interacting with one another. For example, the collision of billiard balls was a common interaction to study. These experiments lead to documentation on the hardness of collisions which lead to the understanding that kinetic energy can be transformed into heat. Early percussion research led to large developments in the defense industry and helped create weapons. From percussion research, in 1687, Newtons Principia was proposed. Newton proposed that sound propagates from one molecule to another. This was the first known study done on an atomic level. Newtons study sparked the interests of other naturalists and a snowball effect was created. Cassini, Jr. in 1707, invented the first ballistic pendulum from the

Law of the Conservation of Impulse. From this invention, the velocity of a projectile was calculated quantitatively for the first time [1].

Simeon Denis Poisson is considered to have begun the era of shock waves in 1808 [1]. Following Poisson, numerous well known scientists have worked in the field of shock physics.

The study of shock waves came from many disciplines which came together to create a new field of science. Shock physics became more prominent in the early 1900s when an increase in warfare and competition between countries created a race for knowledge.

The study of shock waves in water specifically has large applications in the medical field, planetary sciences and geophysics, and the defense industry. The understanding of water's shock response has been underway for over five decades [2]. The medical field studies shock wave in water at very low pressures. The defense industry has interest in studying shock waves in the low and high pressure range. Planetary scientists and geologists study shock waves mainly at high pressures.

Shock pressure pulse waves in medicine is a rather new but important field [6]. Human tissue is comprised of about 70% water so understanding how shock waves interact in water can be helpful in medicine [7]. Water's shock impedance is considered to be close to living materials so tests on water are enough for a medical test [2]. Currently, there are multiple ways of inducing a shock in living tissues without damaging the healthy tissue. One such method is by the use of lasers to create shock pulse waves in the living tissues. To create a high pressure shock wave for a minimal duration of time

to aid in the destruction of unwanted tissues in the body a laser surgical probe has been developed. This method has been tested in patients with proliferative diabetic retinopathy to remove blood clots near the retina [8]. Shock waves have become the treatment of choice to dismantle kidney and ureteral stones in the body [9]. They have also been used to treat humans as well as race horses with tendinopathies. When the injured area is treated with a shock wave, the healing process is boosted by revascularization [9]. Shock waves in medicine have allowed what would normally be an invasive surgery to become minimally invasive.

Compared to the use of shock waves in other related fields, in medicine the wave must be in the range of a few joules to a few milli joules per shot [6]. The goal of the medical application is to only shock the tissues that are damaged and allow the healthy tissues to be left alone. If proper precautions are not taken, the patient can experience unwanted side effects such as cells rupturing and hemorrhaging [10]. To keep the patient safe, the energy of the shock wave has to be kept to a minimum. Low pressure shock waves have been studied for the medical field but have unreliable results [6]. Due to the lack of reliable shock wave data in the medical field, studying shock waves is of special interest and importance currently.

Seemingly close to the use of studying shock waves in water for the medical field, it is also important for the global health sector. Shockwaves can purify water by removing 99.99% of salt from water. This occurs through an electro dialysis shock system which sends current through water. This current separates the salt enriched water from the salt depleted water. This system of purifying water also can remove other unhealthy minerals like copper, boron and lead [3]. While this is an expensive way of

purifying water, with additional research and developments in technology, it would help make the ocean water more useful to humans.

Scientists have also studied wave propagation at extremely high pressures with a range of materials to benefit the defense agencies and planetary scientists. Regan et. al. used neutrons from an underground nuclear explosion to create a high-pressure shock in molybdenum. This was done by fission heating a slab of uranium adjacent to the molybdenum. Regan et. al. determined the Hugoniot, shock velocity, and particle velocity of molybdenum at 2 TPa. This experiment was the first of its kind to study shock waves at a pressure region near 2 TPa. [11]

Lyzenga et. al. measured the temperature of shock compressed water. At pressures from 50-60 GPa, the temperatures measured between 3300 and 5200 K [12]. Lyzenga, et. al. used a six channel optical pyrometer to perform the temperature measurements of the shock with the assumption of constant volume.

Sarah T. Stewart, at the University of California at Davis, has studied the effects of a shock front in water ice. Her studies primarily focus of planetary applications. In one study, she looked at shock induced melting of H₂O ice. To complete this study, a 40 mm polycarbonate projectile was launched via compressed air at an ice disc target. Stewart was able to derive an ice Hugoniot that has applications in the majority of the solar system. From this study, Stewart was able to derive critical shock pressures that are required to initiate and complete melting of ice on a planet [13].

In a further study, Stewart studied the thermodynamics of impacts of collisions between icy planetary bodies. Stewart was able to measure the dynamic strength and

shock states of ice. The Hugoniot that Stewart determined includes five regions of ice phases in Figure 9 . Stewart mapped elastic shocks, deformation shocks and shock transformations of liquid water. During this study, Stewart noted that the low-pressure region of shock has been difficult to interpret. However, the high-pressure region of the ice Hugoniot, which is greater than 8 GPa is well characterized [14]. Further research needs to be conducted in the low-pressure spectra.

Similar to the study of Hugoniot of ice in the low-pressure region, the study of water in the low pressure region needs to be further characterized. There have been many reports of shock Hugoniot data for water in the region below 2 GPa. However, there is variation in the results of the data leading one to believe there is something inherent about water scientist have yet to understand. The following paragraphs will describe shock studies at low pressures of water. These scientists work will be compared to the experiment conducted on water at Marquette University.

M. A. Cook et. al., created shock fronts in water with point-initialed charges rather than a compressed gas gun. The scientists used an “Aquarium Techniques” to find an equation of state for water. The “Aquarium Techniques” uses a rotating streak camera and an explosive flash bomb to collect data. They were able to find the change in time and distance to obtain a shock velocity value using images similar to Figure 1 [15]. Since water is transparent, this technique is possible. The height of the water sample or a higher detonation pressure from the shock-generator charge could be adjusted to obtain a higher shock velocity. This technique is reliable for release waves and shock waves [15]. The experimental results associated with this study are presented in Chapter 6.

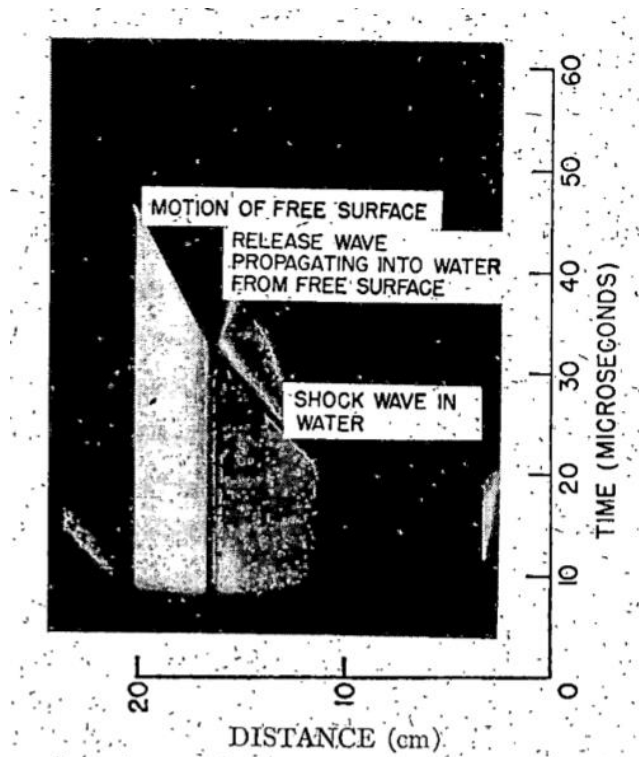


Figure 1: Experimental image used to determine shock velocity [15].

In an experiment published in the Review of Scientific Instruments, Mori et. al. studied shock waves at pressure less than 2 GPa. Their interest developed from the lack of low pressure data that is needed to estimate the shock pressure pulse generated in biological tissues. The experiment was conducted on a compressed gas gun with a 40 mm bore diameter, pulsed laser light, and a high-speed camera. The scientists used a newly designed experiment with a triangular optical prism on the back surface of the water. Light from a laser beam is reflected via total internal reflection prior to the experiment. As the shock front passes through the water sample, the refractive index changes. This shift in the refractive index causes the light to refract into the water rather than reflect into a sensor (Figure 2) [2]. The data associated with this is demonstrated in Chapter 6.2. The team determined that their new method is reliable.

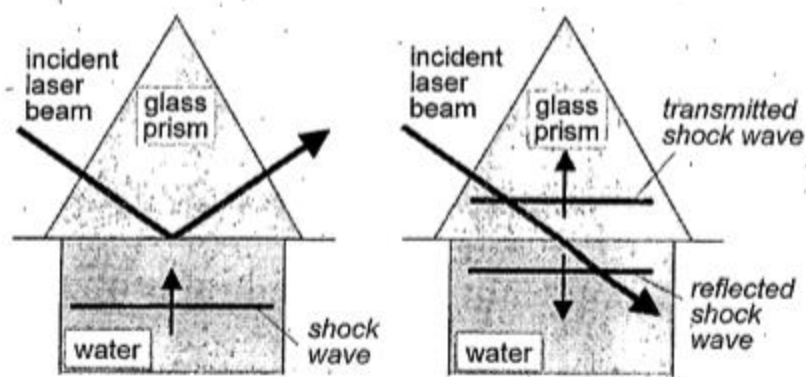


Figure 2: Demonstration of the experimental analysis for Mori et. al [2].

Using the same experimental setup as Y. Mori et. al., K. Nagayama et. al. measured a compression curve for water up to 1 GPa. The experimental setup is demonstrated in Figure 3. When conducting the experiment, distilled and boiled water was used as the test sample. This was done because the group recognized other water contained gas bubbles and minerals that can infringe on the experimental results [4]. The results were acquired using a similar method as Cook et. al. with a high-speed camera images (Figure 4). The team verified that shock-particle velocity Hugoniots can be described by a linear line with a large slope. The large slope is the result of the compression of the water sample [4].

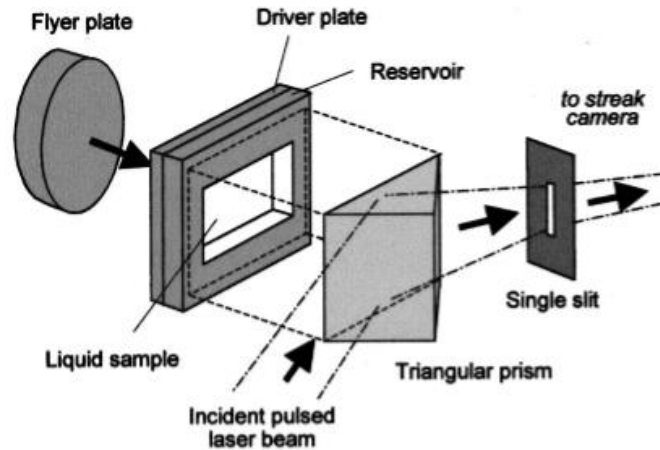


Figure 3: Experimental set up [4].

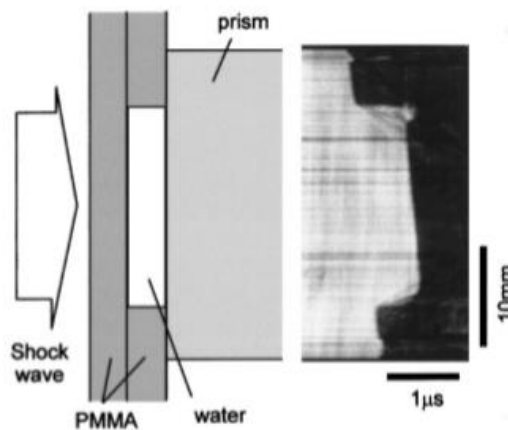


Figure 4: Experimental image used to determine the shock velocity by Nagayama [4].

P. C. Lynse is interested in low pressure data for water saturated tuffs. This data is used to study meteorite impacts and underground detonation. High pressure data has already been experimentally determined and verified but low pressure data is required to study larger volume samples of ground. Lynse used the experimental set up demonstrated in Figure 5 with a gas gun. Distilled water from an ice bath is filtered into the target continuously during the experiment. An aluminum cell is struck by a projectile which

provides a trigger to an oscilloscope to determine the shock velocity. On the back surface of the water sample, a quartz gage is in contact with a shorted guard ring that send signal to an oscilloscope [16].

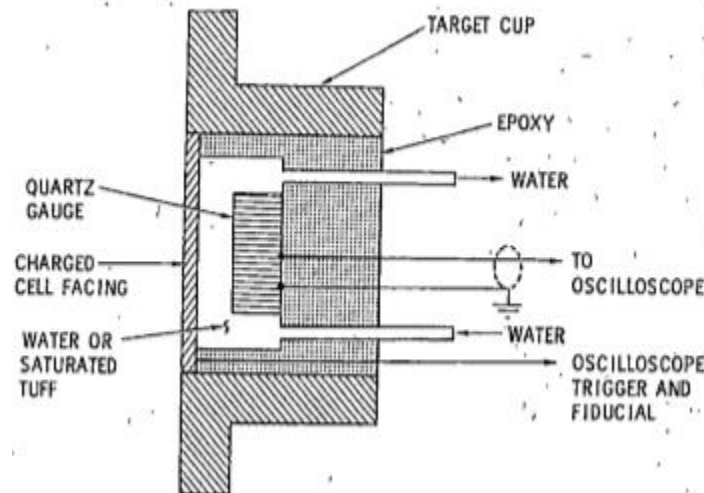


Figure 5: Lynse experimental setup [16].

Sharipdzhanov et. al. focused on water research for the application in power engineering. The study was conducted to determine a Hugoniot at pressures up to 1.4 GPa. The experimental data was graphed and is shown in Figure 6. The group found that the graph of shock velocity versus particle velocity is comprised of two lines with different slopes and a noticeable ‘kink’ in the data known as a phase transition. The phase transition occurs between the particle velocity of 1.84 and 2.13 m/s and at a pressure of 9 and 11.5GPa. This kink in the data has been observed by other scientists. Many have different opinions as to what causes the kind [17]. One such author proposed the kink is caused by the water shifting from liquid to ice VII [18]. Sharipdzhanov proposed that the

kink is caused by water resembling fused silica which can have modifications of its structure [17].

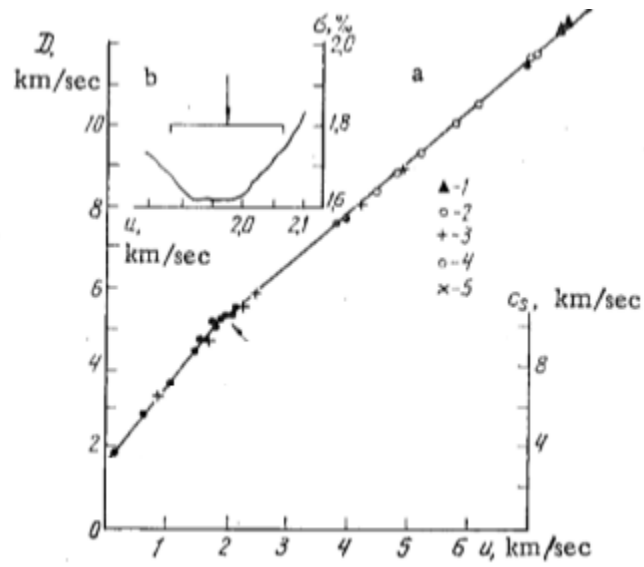


Figure 6: Experimental results depicting a kink in the data [17].

3. Theory

3.1 Water: A Brief Overview

Water is important because without water, life on earth would not be possible. Water, or H_2O , covers 71% of the earth's surface and makes up 96.5% of the earth's crust [5, 9]. Also, there is approximately 13 trillion tons of water in the atmosphere as well [4]. All forms of life depend on water in either liquid or vapor form. Water may not contain organic nutrients or calories but it is essential in powering the human body. The economy also runs on water for most major industries, whether it be growing agriculture or running power plants. Because of water's prevalence, understanding how it behaves under extreme conditions is an important aspect of understanding extreme events such as earthquakes, impacts and explosions that encompass water.

Water has three phases: solid (ice), vapor, and liquid, and multiple phases within the solid phase. Water possesses an unusually complicated phase diagram. It is a non-linear and polar molecule that appears at the end of chemical reactions frequently [5, 10]. What makes the water molecule unique compared to other molecules is its structure, shown in Figure 7. Water has four hydrogen-bond sites, two for accepting electrons and two for donating electrons [19]. These sites allow the water molecule to change into many different states and form new bonds.

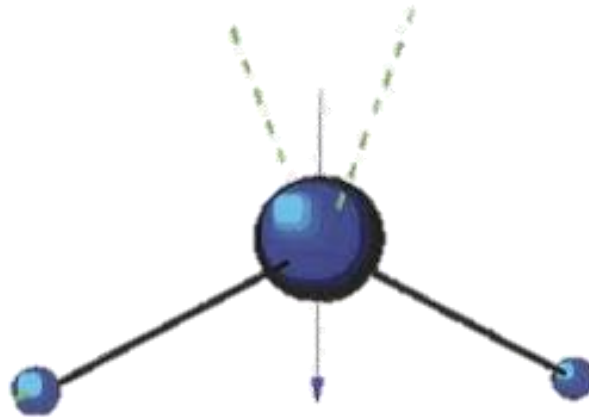


Figure 7: A schematic of a water molecule in the liquid state.

Water vapor is also necessary for a variety of life forms. Water vapor radiates and transfers heat from the sun. As heat radiates off of the earth's surface, it is absorbed by water vapor molecules in the lower atmosphere. These molecules radiate this heat in all directions and then rise to the upper atmosphere. The water vapor will then condense to clouds and cool off. Once the clouds cool off, the water vapor turns to snow crystals or rain and the process is repeated [20]. This cycle allows heat energy to be transferred around planet earth. In the industrial age, more water vapor is being created by factories and automobiles and could be a contributing factor to the global warming of earth.

Ice is the most complex form of the water molecule as it has more than 15 many possible states. Ice is formed when the number of hydrogen bonds is equal to the number of covalent bonds [19]. When this occurs, the Van der Waals forces between the molecules become negligible. This phenomenon only occurs in the water molecule alone [19]. Ice forms a tetrahedral form shown in Figure 8.

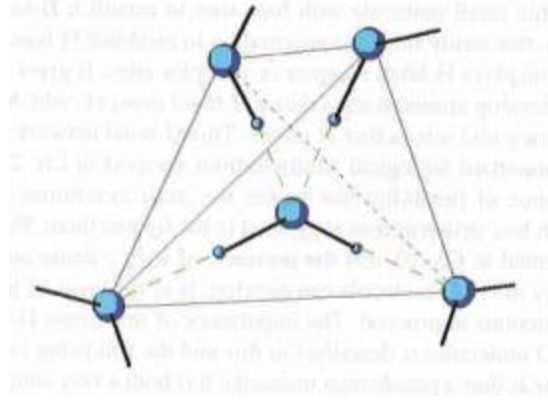


Figure 8: Tetrahedral molecular form of ice [19]

The seven different forms of ice are dependent on temperature and pressure.

Below shows a graph of pressure versus temperature for the different forms of ice (Figure 9).

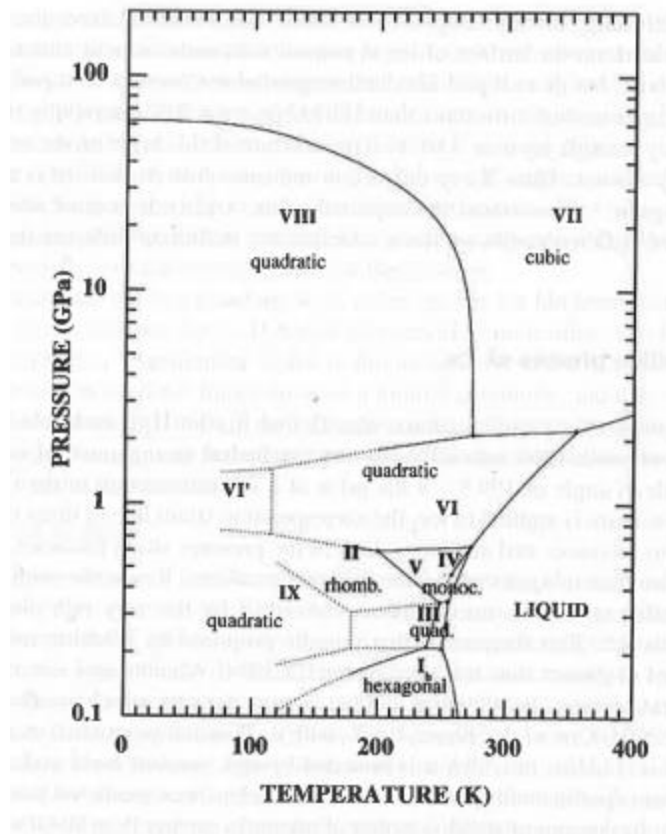


Figure 9: Pressure (GPa) versus temperature (k) of the ice forms [19]

Shown on the graph between 100 and 200 kelvin is ice hexagonal or “Ice Ih”. Ice Ih is the most common form of ice, and is the traditional form humans are aware of. Ice Ih is in snow crystals, ice cubes, freezers etc. The lower pressure ice forms are Ice II, Ih, III, IV, V, and IX. These forms of ice are open structures [19]. High pressure ice differs from the low pressure ice because it is no longer an open structure connected through hydrogen bonds. High pressure ice also has a higher density compared to the ice at low pressures [19]. Figure 9 demonstrates that increasing the pressure of the ice increases the melt temperature.

The water molecule is unique compared to other liquids in the solid phase. As ice is formed, it becomes less dense than water. At about 4 °C, the molecular structure has a density of 917 kg/m³, while its liquid form density is about 1000 kg/m³ [5]. While this differential may seem unusual, it is an exceptional property of water. It is the reason ice floats in a glass of water and on top of the ocean.

The chemical properties of liquid water outperform similar molecules. Liquid water has the unique ability to dissolve cations and anions and ionize acids and bases [19]. The hydrogen bonds that have two acceptor and two donor sites are more flexible in liquid water than in ice. This flexibility results in other molecules becoming embedded into water and salts solvating with ease. Depending on the temperature of the water, the speed of sound in water is around 1400 m/s to 1540 m/s. Through the understanding of water's speed of sound, technologies such as sonar have been developed [5].

Water also features exceptional physical properties both in the static and dynamic form. First and foremost, the density of water is dependent on the temperature of its current state. Shown in Figure 10, one can see a plot of density versus temperature.

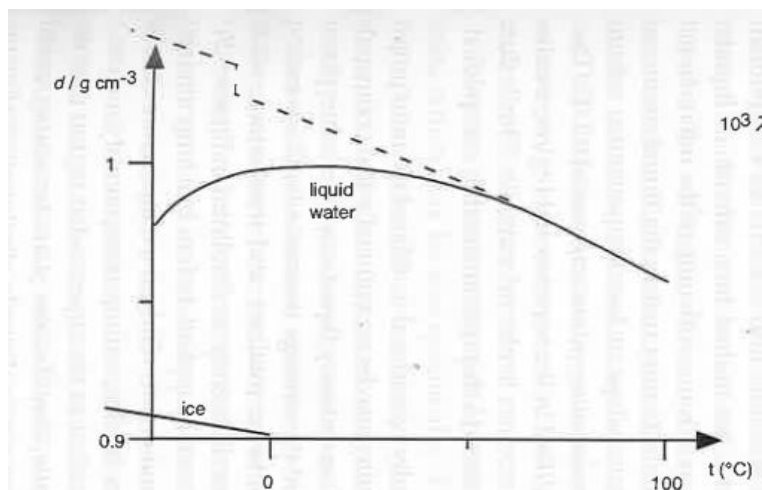


Figure 10: Density versus temperature for water in the solid line [19]

The dashed line shows the typical trend of a molecule, which is a downward slope. Water is represented in the solid line on the graph [19]. Liquid water first displays an upward trend and it peaks around 5 °C. At 5 °C, the curve becomes downward sloping mimicking the pattern of other molecules. This phenomenon explains why ice is less dense than liquid water, its most unique property.

The second static physical property of liquid water is its isothermal compressibility [19]. Isothermal compressibility is the ability to compress a collection of molecules under a given volume. As the isothermal compressibility value increases, the molecule compresses with more ease. Water deviates from the normal pattern compared to other molecules as it slopes downward, then upward. Figure 11 demonstrates this pattern through a graph of the isothermal compressibility, X_T , versus temperature, T .

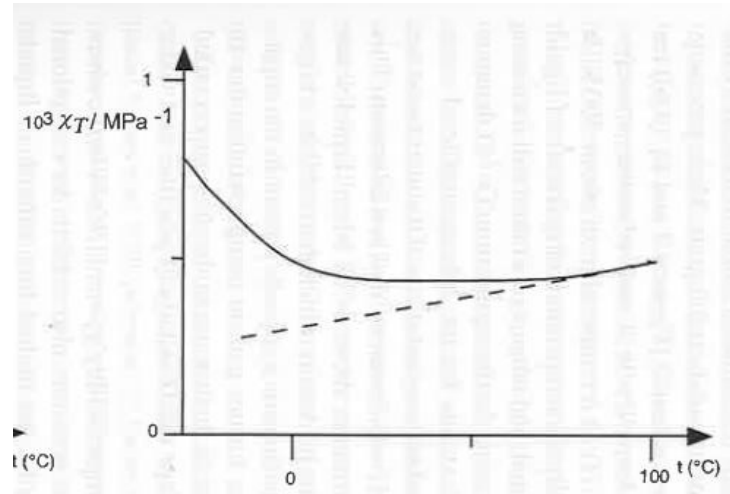


Figure 11: Isothermal compressibility, χ_T , versus temperature, t [10]

Figure 11, was modeled off of one mole of liquid water [19]. The isothermal compressibility for water begins with a downward slope. Similar molecules follow only a positive upward slope throughout the entire course of this graph while water does not. Before 50 °C, water becomes less resistive as temperature increases. Around 50°C, the water begins to follow an upward trend with a positive slope. As this occurs, water becomes more resistive to compressing. This occurrence of having a higher compressibility coefficient is directly due to water being less dense at lower temperatures and more dense at higher temperatures [19]. More dense materials are more restrictive to compressing.

The third physical feature of water is a dynamic feature involving its viscosity, η . For most liquids, as a pressure is applied at a fixed temperature, its viscosity increases. This occurs because as pressure is applied to multiple molecules in a fixed volume; the distance between each molecule decreases, resulting in a more viscous liquid [19]. When liquid water is at temperatures below 50 °C, the viscosity value begins to decrease until it

reaches a pressure around 100 MPa [19]. Once the pressure is about 100 MPa, it begins to increase and follow the trend of most liquids. This is demonstrated in Figure 12, showing the viscosity versus pressure.

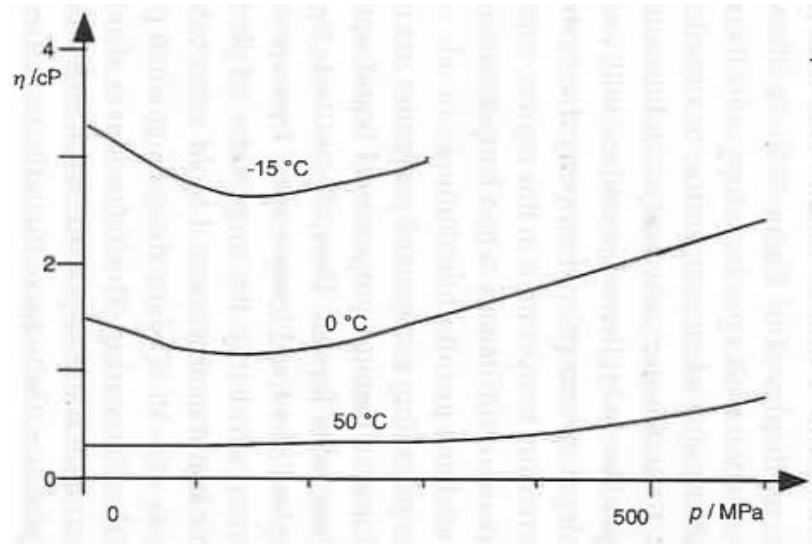


Figure 12: Viscosity versus pressure of liquid water at three fixed temperatures [10].

This change in viscosity is due to the chemical structure of water. As pressure is applied to the molecule, its hydrogen bonds bend [19]. When the hydrogen bonds begin to bend, the molecule will bind to neighboring molecules and become more fluidic [19]. As the H-bonds bend, the O-O distance shortens. Once the O-O bond shortens, water begins to act like similar liquids. This is shown in Figure 9, when water begins following a positive slope at pressures over 100 MPa. The O-O distance shortening is also the cause for the negative slope between liquid water and Ice Ih in Figure 9.

Water's diffusivity coefficient, D , also behaves differently than other liquids at lower pressures. Diffusion is the transport of molecules from one substance to another

substance [21]. Therefore, the diffusivity constant of a material is a measure of a materials ability to allow a substance or energy source to diffuse though its molecules [21]. In most liquids, as pressure increases, the diffusivity coefficient decreases [19]. Shown in Figure 13 , is liquids water’s diffusivity trend in the solid line compared to similar liquids in the dashed line.

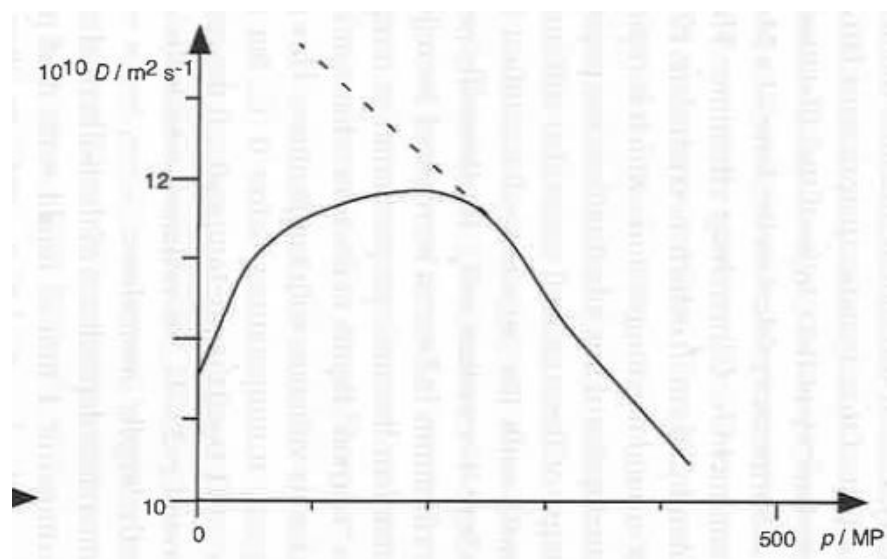


Figure 13: Diffusivity versus pressure for liquid water [10]

Water’s diffusivity increases until around 200 GPa and then it forms a negative slope.

The reason for this positive slope is the same reason for the water’s viscosity trends. As the pressure increases, the hydrogen bonds of the water molecule become more flexible and allow more substances or energy forms to pass through [19]. Water has exceptional physical and chemical properties that allow it to behave differently than other like materials. While to most humans water is seemingly simple, it is more complex than most other molecules.

3.2 Shock Wave Overview

Shown in Figure 14, is a typical stress-strain curve. The strain measures the amount of deformation placed on a material, while the stress measures the force applied to the area of a material. For most materials, the stress-strain curve is linear until the yield point. The yield point represents the transition from the elastic to plastic behavior in a material. Once the material has reached its particular yield point or elastic limit, the material will no longer return to its original form. When the material exceeds the elastic limit, part of the material is under permanent deformation which is known as plastic deformation [22].

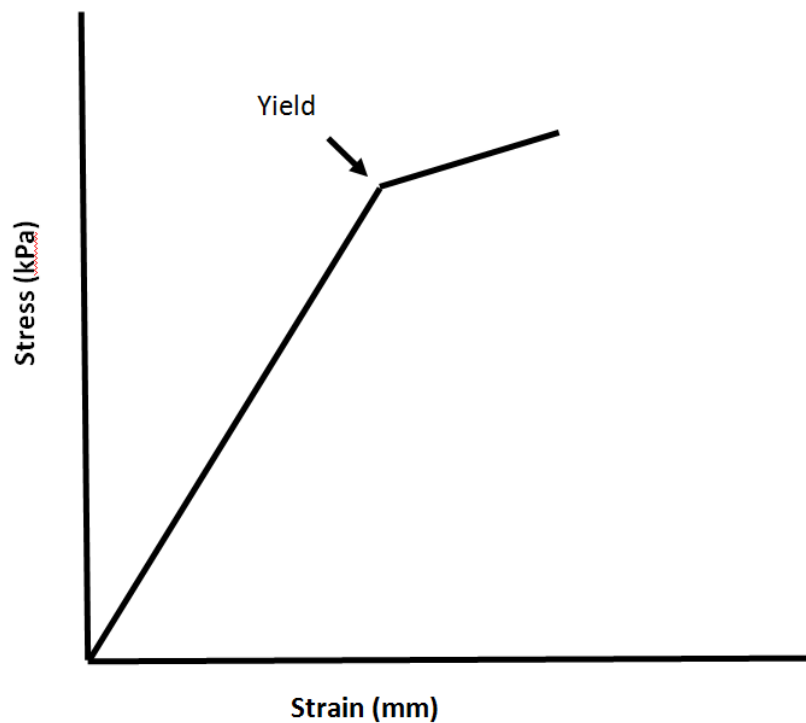


Figure 14: Typical stress versus strain graph.

In a tensile test, a material specimen is pulled in at a known tension until the material reaches above its yield point and failure occurs. In the experiment described below, a material is stressed beyond its yield point at much higher loads than a standard tensile test. A single stage gas gun at Marquette University was used to stress water beyond its yield point by passing a shock wave through it. This field of study called shock physics.

Shock physics is the study of compressive stress and strain on a material [22]. For simplification purposes, only uniaxial stress and strain will be considered. Uniaxial stress and strain shows only the material axes that are perpendicular to the strain axis making it infinite and eliminating edge effects.

There are three zones located on the stress-strain curve shown in Figure 15. In Zone I, the material can return to its original shape when released, otherwise known as the elastic zone. In the elastic zone, the sound velocity is constant for the material and the pressure and density are linearly related. Zone II is the elastic-plastic region where the material's behavior is dependent on pressure and shock velocity. As the velocity increases the pressure will also increase, it is no longer constant. The third and highest zone is the overdriven zone. This occurs when the material is stressed above its yield point and the material becomes permanently deformed [22]. When studying water, it is always studied in the over driven zone. This is because water does not have a yield strength so the Hugoniot elastic limit, which is the line separating Zone I and II is nearly

zero because of water's lack of yield strength. This drives the graph down so the water can be studied in Zone II or III.

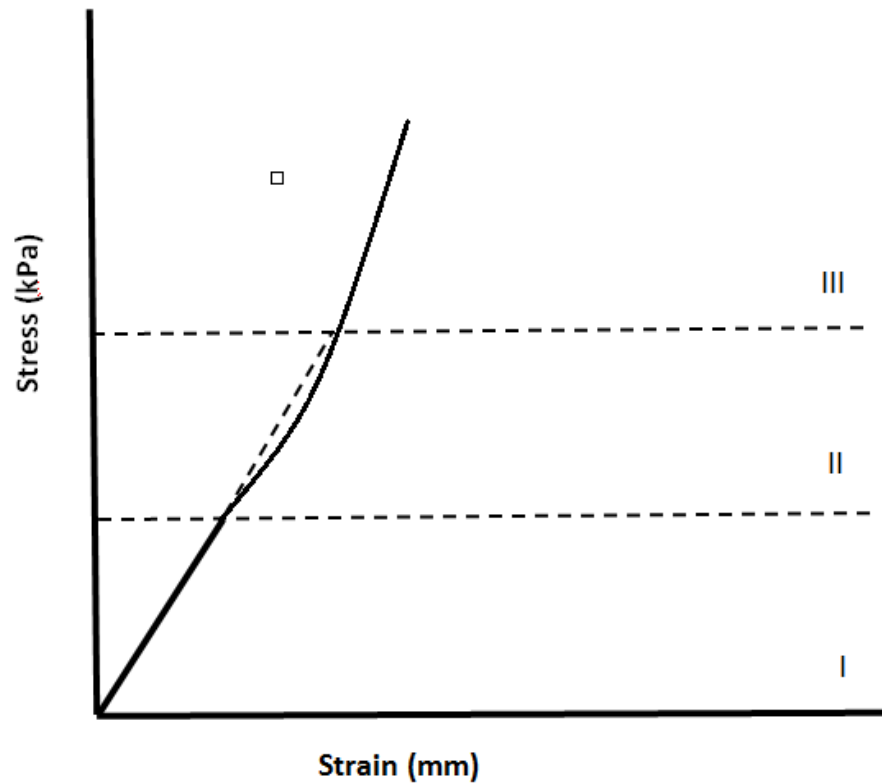


Figure 15: Typical stress versus strain graph with the three zones labeled

Shock waves occur when a pressure wave travels through a medium faster than medium's speed of sound. Oxford Dictionary characterizes a shock wave as "a sharp change in pressure in a narrow region travelling through a medium, especially air, caused by explosion or by a body moving faster than sound." [23]. When a shock wave occurs, there is an extreme change in temperature, pressure, and density in the medium it is traveling. Shock waves can travel in liquids, solids, gases, and electromagnetic fields.

The waves can be normal, oblique, or bow to the surface of the shock front [24]. For the purposes of this study, only normal shock waves will be considered. Normal shock waves occur perpendicular to the flow direction of the medium.

A Mach number, M , is used to describe the ratio between the local speed of sound, c , and the speed of the object, v , that is in flight [25].

$$M = \frac{v}{c} \quad (1)$$

The Mach number helps classify the wave as transonic, subsonic, or supersonic. A transonic wave has a Mach number near one which is approximately equal to the local speed of sound. A subsonic wave has a Mach number less than one and it travels slower than the speed of sound. Thus, a shock wave will not be created but in a lab setting it can be simulated using experimental data and impedance matching. This method will be further described later. A supersonic wave has a Mach number greater than one and travels faster than the speed of sound. Supersonic waves are shock waves and have the ability to transfer the shock wave into an object which it strikes. Supersonic waves vary with amplitude. If the wave's amplitude decreases, then the speed of the wave will also decrease [25].

When studying shock waves, it is essential to know the shock velocity and particle velocity for a given experiment. The shock velocity is the velocity of a wave moving through particles. The particle velocity is the velocity of one individual particle moving. The shock velocity always travels at a faster velocity than the particle velocity as seen in Figure 16. The yellow block is the initial disturbance which comes into contact

with the black boxes. The yellow box's velocity is the particle velocity. The shock velocity propagates through each box and is transmitted into each additional box when they come into contact.

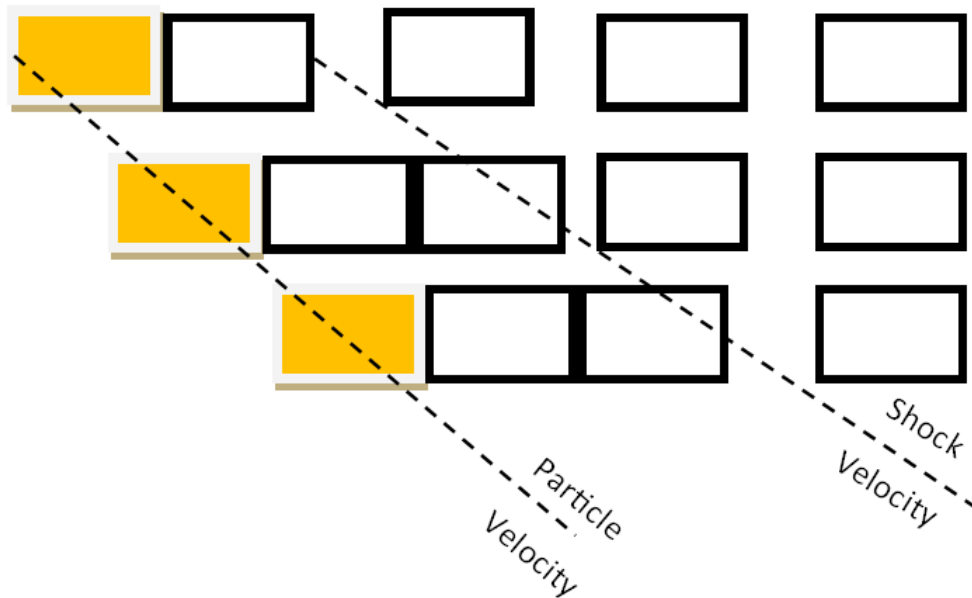


Figure 16: Demonstration of the travel times of the shock and particle velocity.

When a projectile comes into contact with a target, a wave front is transmitted. The left going wave is known as a rarefaction wave or release wave. A rarefaction wave lowers the pressure of the shock front. Eventually, the pressure will be low enough that the shock wave will return to a sound wave and be in the elastic region. This occurs because a rarefaction wave, that is traveling in a more dense material, travels faster than the shock front. When designing an experiment, simulations should be done to ensure the

rarefaction wave does not reach the shock front before the front completely passes through the sample of interest. The left and right going waves are visualized in Figure 17.

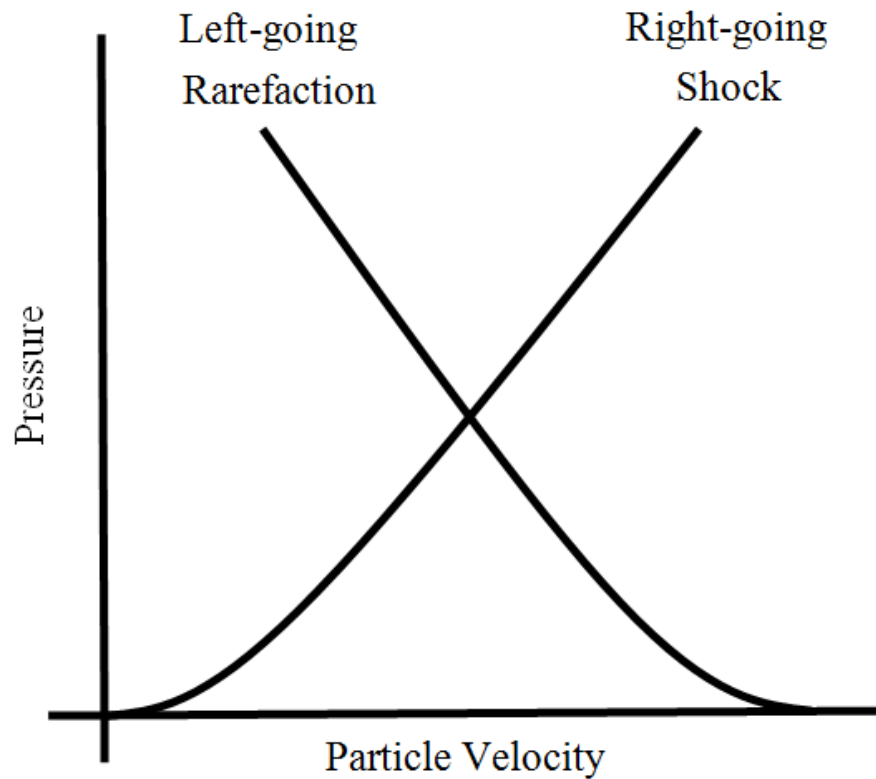


Figure 17: Demonstration of a left and right going wave in pressure-particle velocity space.

To characterize a shock wave and the material's response to a shock wave, the Hugoniot equations are implemented. The goal of the Hugoniot equations is to solve for the shock velocity and particle velocity of a shock wave in a water target. Once the shock and particle velocity are known, a multitude of other variables can be determined. Along with the potential to solve for other variables, a mass, momentum, and energy balance is

applied in the Hugoniot equations. After finding the shock and particle velocity, a Hugoniot line will be determined and compared to published data.

3.3 The Hugoniot Equations

In order to characterize a shock wave, four variables can be used: pressure (P_o), internal energy (E_o), particle velocity (u_o), and density (ρ_o). Variables with the subscript '0' indicate unshocked material and the subscript "1" indicate shocked material. For example, P_o is the unshocked material pressure and P_1 is the shocked material pressure. All four of these variables increase rapidly once the material is shocked. The Rankine-Hugoniot Equations and an equation of state (EOS) will be used to characterize the shock wave. The Rankine-Hugoniot equations depend on the initial and final states of the material. The Hugoniot equations are three conservation equations: a mass balance, energy balance and momentum balance [22].

The mass balance begins by implying the conservation of mass law which states that mass will not be created nor destroyed during the experiment. In the mass balance, v_o is the specific volume and U is the shock velocity [22].

Mass Balance:

$$\frac{\rho_1}{\rho_o} = \frac{U - u_0}{U - u_1} = \frac{v_o}{v_1} \quad (2)$$

The energy balance is formed off of the basis that the amount of work being done on the control mass is equivalent to the energy increase on the same control mass. In Equation 2, E is the internal energy and P is the pressure of the system [22].

Energy Balance:

$$E_1 - E_o = \frac{1}{2}(P_1 + P_o)(v_o - v_1) \quad (3)$$

The momentum balance states that in order for the mass to go from an unshocked to a shocked state, the change in momentum must be equal to the force applied [22].

Momentum Balance:

$$P_1 - P_o = \rho_o u_1 U \quad (4)$$

3.4 The Hugoniot Planes

There are six possible planes of reference that shock wave relationships can be studied in. These planes include shock velocity-particle velocity (U_s-U_p), pressure-shock velocity ($P-U_s$), pressure-particle velocity ($P-U_p$), shock velocity-specific volume (U_s-v), particle velocity-specific volume (U_p-v), and the pressure-specific volume ($P-v$) plane. Of the six possible planes that one can plot data in, the three most useful planes are the U_s-U_p , $P-v$, $P-U_p$ planes.

The relationship between shock and particle velocity is often times a linear relationship for many materials not undergoing a phase transition. In this plane, a

Hugoniot line can be created from a graph. The Hugoniot line is an area or locus of points around which all of the possible equilibrium points for a material can exist [22]. It is important to not confuse the Hugoniot as a materials definite path. A linear Hugoniot is created from Equation 5.

$$U_s = C_o + SU_p \quad (5)$$

In Equation 5, U_s , C_o , S , and U_p , are the shock velocity, bulk sound speed of the material, slope, and particle velocity. U_s and U_p can be defined from experimental results and through impedance matching (See Chapter 6), and then plotted. Through the plotting of U_p versus U_s , with the help of curve fitting tool, a first order polynomial can be fitted to the experimental data. The bulk sound speed, C_o , is the y-intercept of the graph and the slope is found from the line. If the purpose of the research being conducted is not to characterize the material, then there are known C_o and S values available. Paul Cooper's, *Explosive Engineering*, has a table of common materials and their constants. Using these values would allow one to validate their data to a material's Hugoniot line.

In general, the Hugoniot line of a material will be a straight line. If there is a change in the crystal lattice or a phase change in the material of interest, then there will be a shift in slope demonstrated by the Hugoniot [22].

The pressure-specific volume plane eliminates the shock velocity and particle velocity from all equations. To do so, the initial pressure and particle velocity must be assumed to be zero. In this case, the Hugoniot line can be computed from Equation 6.

$$P = C_o^2 (v_o - v)[v_o - S(v_o - v)]^{-2} \quad (6)$$

For the purposes of this research project, this plane will not be used in calculations because the initial pressure of the experiment will not be assumed to be zero.

The final plane is the pressure-particle velocity plane. An assumption was made that the pressure of the left going shock wave is the same as the right going shock. The left going shock wave begins when a flyer or projectile strikes a stationary object. At this point, a left going shock is created in the flyer and a right going shock is created in the stationary object. To find the particle velocity, the pressure from the left going shock, Equation 8, is set equal to the right going shock, as seen in Equation 7.

$$P_R = \rho_R(C_R(U_p - U_0) + S_R(U_p - U_0)^2) \quad (7)$$

$$P_L = \rho_L(C_L(U_0 - U_p) + S_L(U_0 - U_p)^2) \quad (8)$$

In Equation 7 and 8, ρ_R , ρ_L , U_p , and U_0 , are the densities of the right and left material, the particle velocity, and the initial flyer velocity. This plane can be helpful in determining the particle velocity of the material to then compare it to the shock velocity. For more information on this calculation and on how to expand it to multiple material interactions see Chapter 3.4 on impedance matching.

For the purposes of this research, the particle velocity will be determined in the P-U_p plane and then further calculations will be conducted in the P-U_s plane. For a better understanding on how this was completed, see Chapter 3.5 and 3.6, below on impedance matching, shock velocity calculations and error analysis.

3.5 Shock Velocity

The shock velocity is a necessary calculation to determine the Hugoniot line and also the particle velocity. To solve for the shock velocity, the distance the shock has traveled and the time it takes to travel through the sample must be known. Combining the two variables, the shock velocity can be solved with Equation 9.

$$U_s = \frac{x}{t} \quad (9)$$

In this experiment, x is a known value of .00172 m for each sample in the experiment. The time value changes for each experiment. The experimental method for determining the time for the shock to travel through the sample is described in Chapter 5.2.

3.6 Impedance Matching

The technique of impedance matching is used to solve for the particle velocity of the shock wave in the water sample. To do this, the $P - U_s$ plane will be studied because both the pressure and the shock velocity are can be experimentally identified or calculated. The following experimental set up was used:

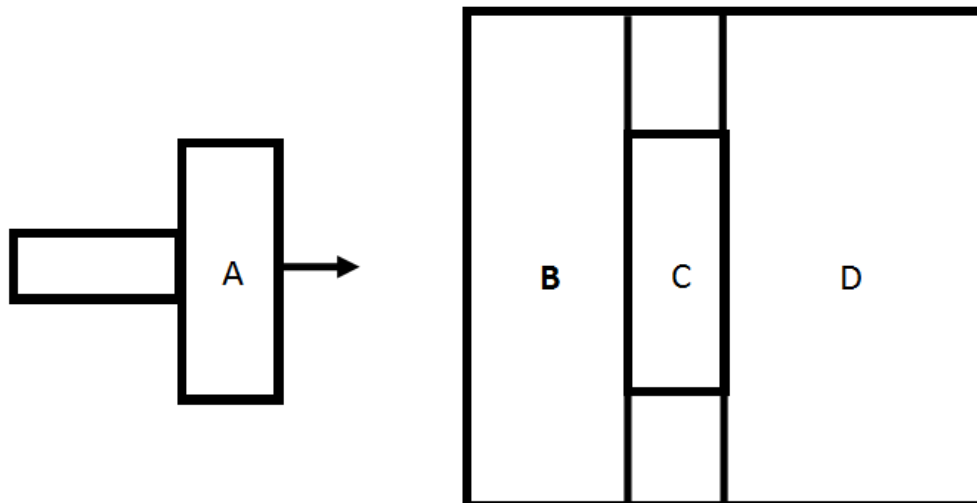


Figure 18: Schematic showing the flyer, A, and target, B, C, and D

In the schematic above, A, B, C, and D are known as the flyer, front anvil, water housing, and back anvil. Material A and B are Polymethyl-methacrylate (PMMA), copper, or aluminum depending on the goal of the experimental set up. Material C is always water that is housed in a PMMA body surrounded by an o-ring to create a tight, leak-free seal. Material D is PMMA. The interaction between A and B must be studied first to determine the interaction between B and C. The pressures of the right and left going Hugoniot are:

$$P_R = \rho(c(U_p - U_0) + s(U_p - U_0)^2) \quad (10)$$

$$P_L = \rho(c(U_0 - U_p) + s(U_0 - U_p)^2) \quad (11)$$

P_R is the right going Hugoniot and P_L is the left going Hugoniot. The variable, C , is the bulk sound speed in meters per second and s is the slope of the Hugoniot line. Setting P_R equal to P_L allows the particle velocity, U_p , to be found. This can be applied to the experiment as follows. Begin by comparing Material A with Material B. Material B originally starts from rest and Material A varies depending on the amount of pressure that is applied to the small gas gun. Customizing Equation 10 and Equation 11 to Materials A and B gives Equation 12.

$$P_{RB} = \rho_B(c_B(U_1 - U_{0B}) + s_B(U_1 - U_{0B})^2) \quad (12)$$

$$P_{LA} = \rho_A(c_{oA}(U_0 - U_1) + s_A(U_0 - U_1)^2) \quad (13)$$

Setting P_{RB} equal to P_{LA} gives:

$$\begin{aligned} \rho_B(c_B(U_1 - U_{0B}) + s_B(U_1 - U_{0B})^2) = \dots \\ \dots \rho_A(c_A(U_0 - U_1) + s_A(U_0 - U_1)^2) \end{aligned} \quad (14)$$

In these experiments, U_{0B} , is zero because the first disc always starts at rest. U_0 is the initial flyer velocity before striking the target. If material A and B are the same material, the Equation 14 would simplify to Equation 15.

$$U_1 = \frac{1}{2} U_0 \quad (15)$$

However, this is not the case for every experiment so simplifying Equation 14 assuming material A and B are different yields:

$$\rho_B c_B U_1 + s_B U_1^2 = \rho_A (c_A (U_0 - U_1) + s_A (U_0 - U_1)^2) \quad (16)$$

Reorganizing Equation 16 and setting it equal to zero puts it in the form of the quadratic formula. Solving for U_1 is possible by substituting the constants from Equations 18-20 into Equation 17.

$$U_1 = \frac{-B \pm \sqrt{B^2 - 4AC}}{2A} \quad (17)$$

$$A = s_B - s_A \quad (18)$$

$$B = \rho_B c_B + \rho_A c_A + 2s_A U_0 \quad (19)$$

$$C = -\rho_A c_A - s_A U_0^2 \quad (20)$$

This interaction is graphically demonstrated in Figure 19 .

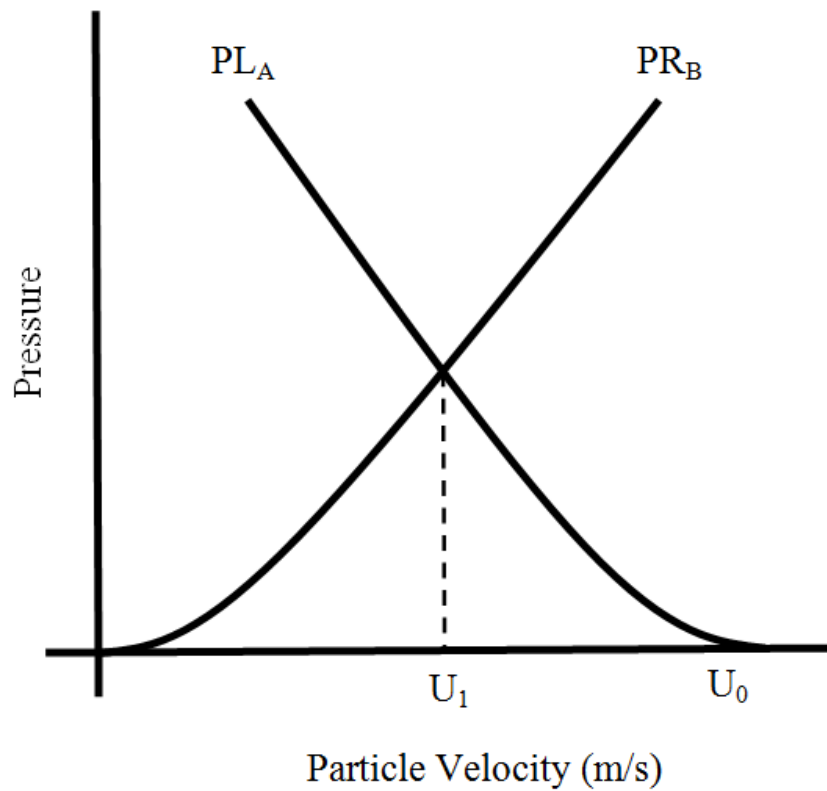


Figure 19: Left and right going waves in the pressure-particle velocity space for target pieces A and B.

Next, the particle velocity between the driver and water interface can be determined using a similar approach as above. Equation 21 and Equation 22 define P_{RC} and P_{LB} .

$$P_{RC} = \rho_c U_s U_p \quad (21)$$

$$P_{LB} = \rho_b (c_b (2U_1 - U_p) + s_b (2U_1 - U_p)^2) \quad (22)$$

Setting P_{LB} equal to P_{RC} gives Equation 23.

$$\rho_c U_s U_p = \rho_b (c_b (2U_1 - U_p) + s_b (2U_1 - U_p)^2) \quad (23)$$

Rearranging Equation 23 gives Equation 24.

$$\rho_b s_b U_p^2 + (\rho_c U_s + \rho_b c_b + 4\rho_b s_b U_1) U_p - 2\rho_b c_b U_1 - 4\rho_b c_b U_1^2 = 0 \quad (24)$$

Recognizing Equation 24 shows that it is in the form of the quadratic formula, U_p can be solved for with Equations 25-28.

$$U_p = \frac{-B \pm \sqrt{B^2 - 4AC}}{2A} \quad (25)$$

$$A = \rho_b s_b \quad (26)$$

$$B = \rho_c U_s + \rho_b c_b + 4\rho_b s_b U_1 \quad (27)$$

$$C = -2\rho_b c_b U_1 - 4\rho_b c_b U_1^2 \quad (28)$$

After solving Equation 25, the particle velocity of the water sample was determined. This is graphically demonstrated in Figure 20. As one can see in Figure 20, when the shock front travels through B and into C, a left going rarefaction wave forms in B and the shock front travels into C.

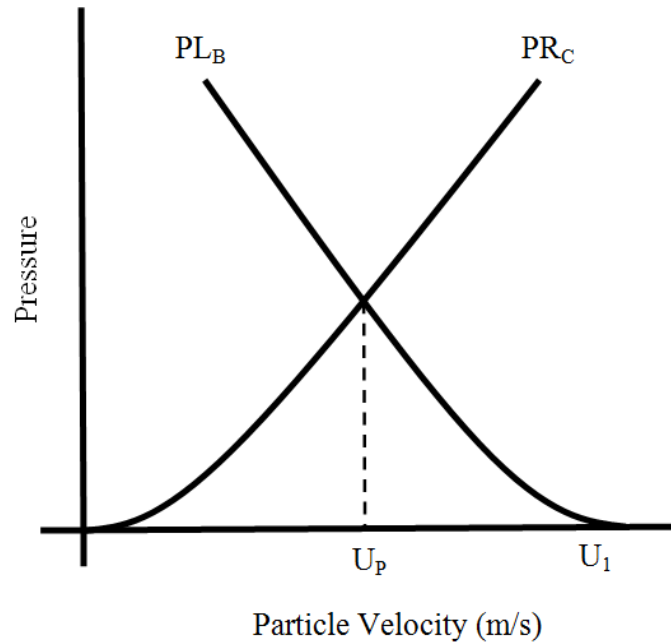


Figure 20: Left and right going waves in the pressure-particle velocity space for target pieces B and C.

After solving for the particle velocity of the water sample, the Hugoniot line of the material to be determined. This is shown in Chapter 3.7.

The process of impedance matching can also be repeated in reverse order to solve for the initial velocity of the flyer. This can be helpful when validating experimental data and models. For this experiment, the impedance matching technique will be completed in the above method only.

3.7 Assignment of a Hugoniot

A Hugoniot line is a locus of possible equilibrium states where a material can exist [22]. This line is determined experimentally by calculating the shock and particle velocity and then graphing these points. After plotting these points, the Hugoniot can be determined from Equation 29.

$$U_s = sU_p + C \quad (29)$$

The variable, C , is the bulk sound speed and the y-intercept of the graph. The slope of the line is “ s ” and is unit less. This Hugoniot line is a first order polynomial. Using Matlab, the data points are curve fit to find the bulk sound speed and the slope of the line. Figure 21 graphically demonstrates the line and Figure 22 shows an output from Matlab.

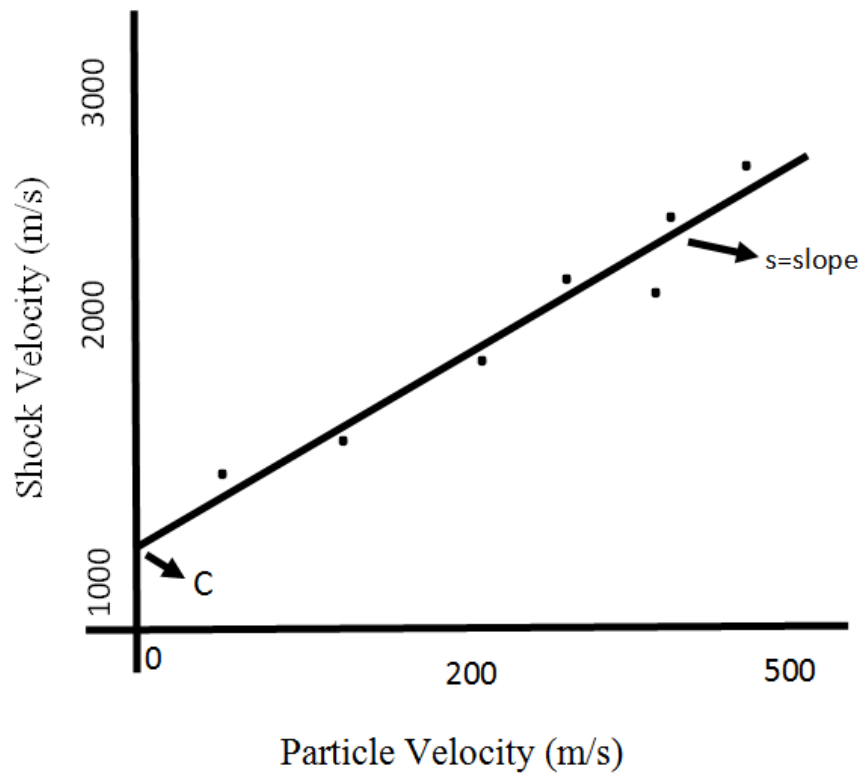


Figure 21: Graphical demonstration of a Hugoniot line in U_s - U_p space

```
Linear model Poly1:  
f(x) = p1*x + p2  
Coefficients (with 95% confidence bounds):  
p1 =    0.1022 (-0.1315, 0.3358)  
p2 =    1681 (1621, 1742)
```

Figure 22: Demonstration of the Curve Fitting Application in MATLAB's output.

In Figure 22, p1, p2, and x is the slope, bulk sound speed and particle velocity. Substituting these values into Equation 29 and solving for U_s allows one to create a line on the shock velocity versus particle velocity graph.

4. Methodology

4.1 Instrumentation Design

An experiment was designed to launch a single projectile through a ½” (12.7 mm) bore single stage gas gun. The projectile made of copper, aluminum or PMMA comes into contact with a target specimen, described in further detail in Chapter 4.2, filled with tap water obtained from Engineering Hall at Marquette University.

The single stage gas gun can reach velocities in a range between 90 meters per second to 320 meters per second. Prior to firing, building provided shop air at 100 psi is compressed by a Haskel Gas Booster (23). The compressed air flows into a reservoir and is isolated from the barrel. The air then reaches the barrel either from a fast-acting solenoid or Mylar burst discs. The fast-acting solenoids restrict the projectiles velocities to 90 meters per second as they cannot switch quickly enough to allow the projectile and the compressed air through. The Mylar burst discs rupture at about 500 psi (3.45 MPa) each and have the ability to increase the launch velocity. Varying the number of burst discs can control the velocity up to the maximum of 320 meters per second. While the Mylar burst discs allow for greater projectile velocities when compared to the fast-acting solenoid, they leave more room for error with repeated experiments. Each burst disc can have slight variations and can cause velocities to ever so slightly change. For the sake of this experiment, the variations in the burst discs is assumed to be negligible.



Figure 23: Haskel Gas Booster

A breach (Figure 25), is pressurized until the Mylar burst disc ruptures. Once the disc ruptures, the compressed air and flyer travel down the barrel of the gun. Following the barrel, the flyer free flies through a stripper box. The stripper box is located between the barrel and the target specimen. Show in Figure 24 below, the stripper box is connected to the target plate by two screws. The stripper box has four graphite break pins that measure the projectile velocity as the flyer breaks each pin (Figure 24). The data is recorded by an oscilloscope. The stripper box has a hole with a diameter smaller than the sabot but larger than the projectile to allow the sabot to be removed prior to impact. This also acts to plug the hole so air cannot flow between the barrel and target during impact. At the end of the stripper box, the flyer is removed from the sabot and strikes the target. The target is encapsulated by a catch tank that acts to catch the shattered target and also stop the flyer from free entering into the room.

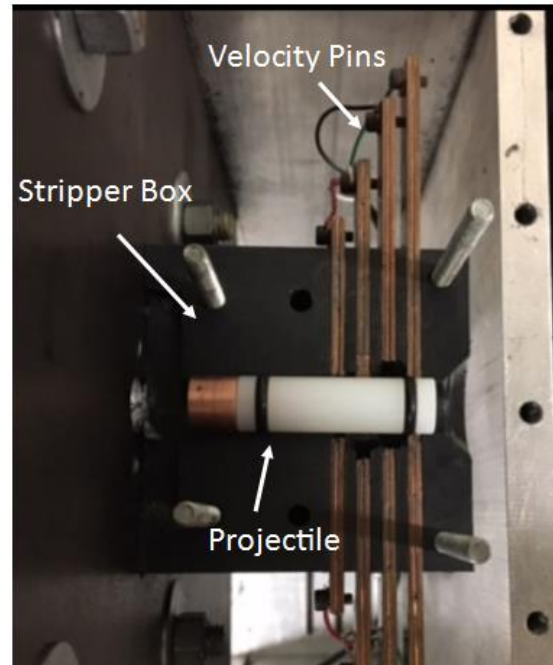


Figure 24: Stripper box, velocity break pins, and projectile

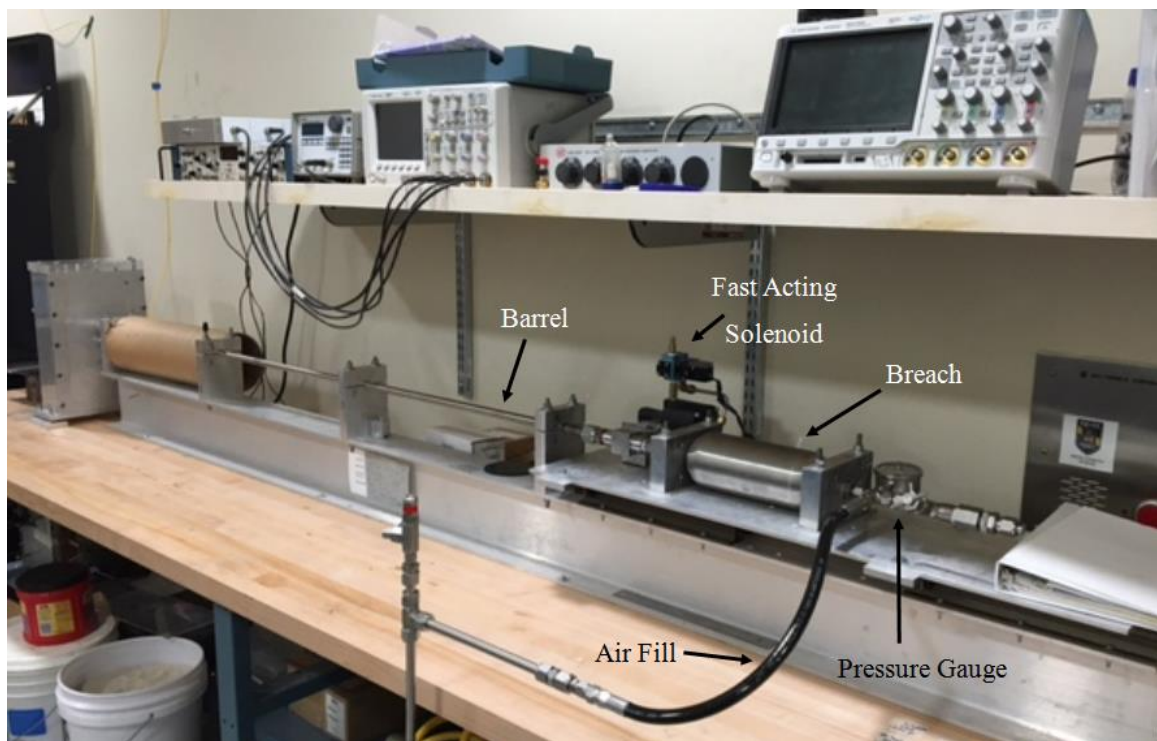


Figure 25: Overview picture of the equipment on the small gas gun

4.2 Projectile Design

The single stage gas gun and target tank are parallel to each other and also to the ground. Since the projectile is guided by a sabot, the experimental set up allows the gravitational effects on the projectile to be negligible. The sabot was CNC machined out of Nylon at Marquette University. The sabot is 1.650 inches in length and 0.475 inches in diameter. It features two 0.080 inch deep cuts where two O-rings are set. A 0.250 inch hole that is 1.00 inch deep is cut out where the tail of the projectile is housed. A cone shape cut out is made in the trailing edge of the sabot that is 0.188 inches deep and 0.075 inches in diameter. This cone shape helps guide the sabot down the barrel and assists with the high pressures at the trailing edge.

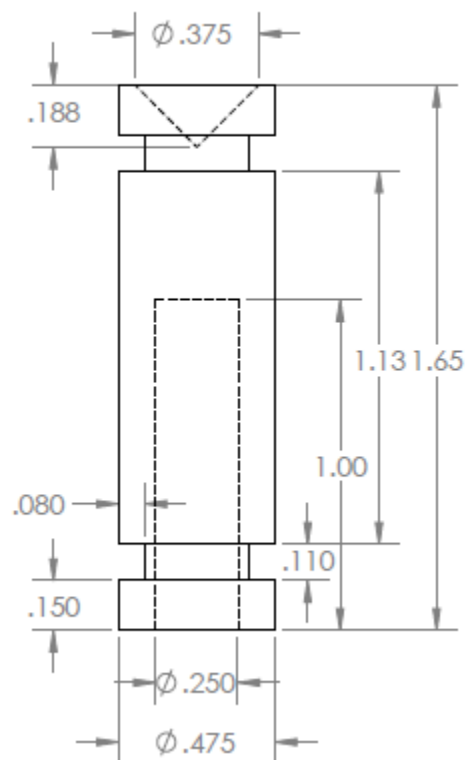


Figure 26: CAD drawing of the sabot design with all dimensions in inches.

The projectile is housed in the sabot until reaching the end of the barrel. The projectile was CNC machined out of copper, aluminum, or PMMA Acrylic. The projectile has two diameters which will be known as the head and tail. The tail of the sabot is 0.25 inches in diameter and 0.59 inches long. The head is 0.48 inches in diameter and 0.39 inches in length. Figure 27 and Figure 28 above show a CAD drawing of a flyer and a copper, aluminum, and PMMA flyer.

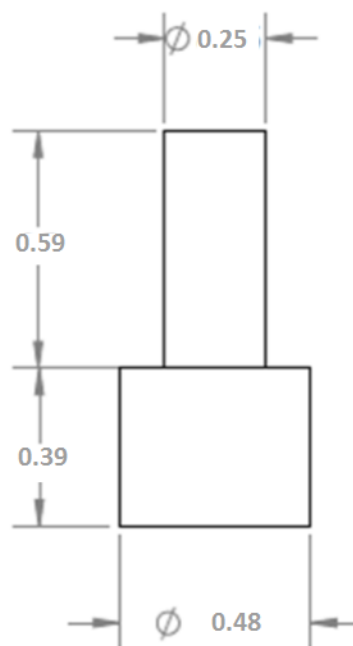


Figure 27: The projectile flyer made from copper, aluminum, or PMMA. Here all dimensions are in inches.

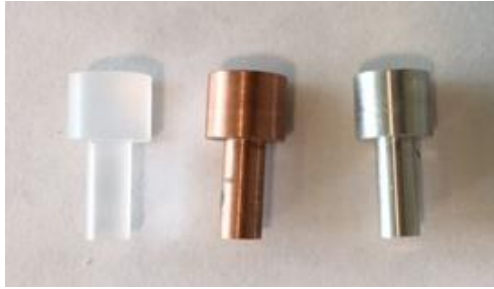


Figure 28: Physical flyers made from (left to right) PMMA, aluminum, and copper

Figure 29 shows the nylon sabot with 2 O-rings and a copper, aluminum, and PMMA flyer inserted into position.



Figure 29: Nylon sabots with two O-Rings and flyers inserted

4.3 Target Design

The target specimen consists of five individual plates that are held together by four 2" #4 screws. Each plate has two additional screw holes that will hold the whole target specimen to the target plate with 2" #6 screws. With the exception of the driver plate, described in further detail below, the plates were constructed out of PMMA Acrylic by an Epilog Laser at the Discovery Learning Center at Marquette University. Figure 30

and Figure 31 show the target assembled and mounted to the target plate and the individual plates laid out.



Figure 30: Target mounted to the target plate

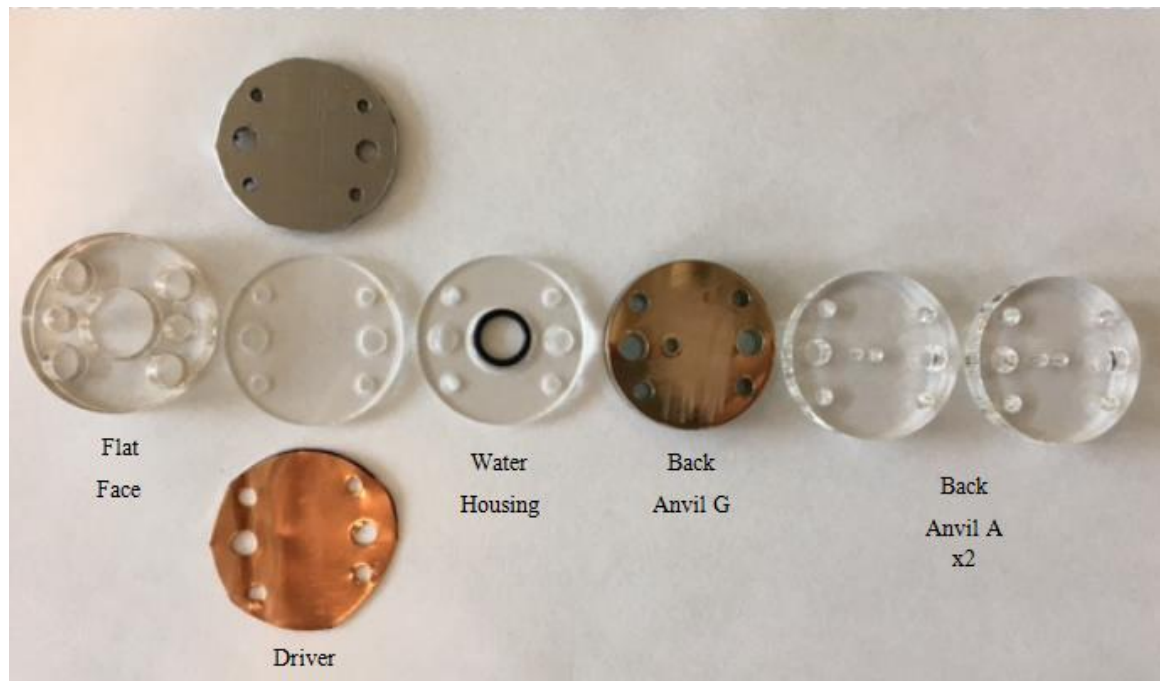


Figure 31: Target components laid out

The first PMMA plate nearest to the target plate allows the plates following it to sit flat against the target plate. This plate is known as the flat plate, and was a necessary feature to the target design due to the four screws that hold the additional plates together. Due to the size and thickness of each plate, the screws were not able to be recessed into the design. The flat plate allows the target to sit flat against the target plate and aligned with the barrel. It features a hole in the center larger than the flyers diameter to create a clear pass through to the target. The plates outer and inner diameter are 1.4" and 0.55". The plate has four holes that all the screw heads to be recessed into the design which are 0.25" in diameter. There is an additional two holes that fit a #6 sized screw.

The driver plate sits just behind the flat plate and is made of copper, aluminum or PMMA. The diameter of the front anvil ranges from 0.01-0.05 inches thick depending on

the material available. The aluminum and copper plates were made in the Discovery Learning Center at Marquette University on a mill. The plates outer diameter is 1.4” wide. The plate has four #4 sized screw holes and two #6 sized holes for screws.

The water housing is constructed from PMMA and is located behind the driver plate. The disc has an outer and inner diameter of 1.4” and 0.50”. The plate is 0.064” thick and again has four #4 sized screw holes and two #6 sized holes for screws. In the center of the plate, an O-Ring sits snugly inside and acts as a seal to the water when compressed between the surrounding plates. The outer diameter of the O-Ring is larger than that of the flyer so it does not interfere on impact.

The final plates are known as back anvil G and back anvil A. Both G and A are 1.4” in diameter and 0.39” thick. Both plates have four #4 sized screw holes and two #6 sized holes for screws. G and A have a hole that is .095” in diameter that is just slightly off center. This hole is the channel for the PZT pin. Back anvil G is sputter coated in gold, for more information on this see Chapter 4.4 . Back anvil A has an additional hole in the center of the plate that is 0.093” in diameter. This channel is for the PZT pin to rest in during the experiment. Following the water housing plate is one G plate and then two A plates.

In the case of copper as the driver plate, an additional plate is needed. This plate is known as the bridge and has the same dimensions as the flat face plate. This plate is needed because the copper used in the experiment is so thin that when compressed between the screws it bows and water leaks out of the target. The plate has a large enough

inner diameter that the flyer passes straight through the flat plate and strikes the copper surface.

4.4 Sputter Coating

A mini plasma sputtering coater manufactured by MTI Corporation model GSL-1100X-SPC12-LD was used to coat the back anvil g plates with gold [26]. The machine, shown in Figure 32, is located on Marquette University's campus in the Dental Research Laboratory. The machine sputters nanometers of a material at a time which is just enough for the reflection of light from the PDV.

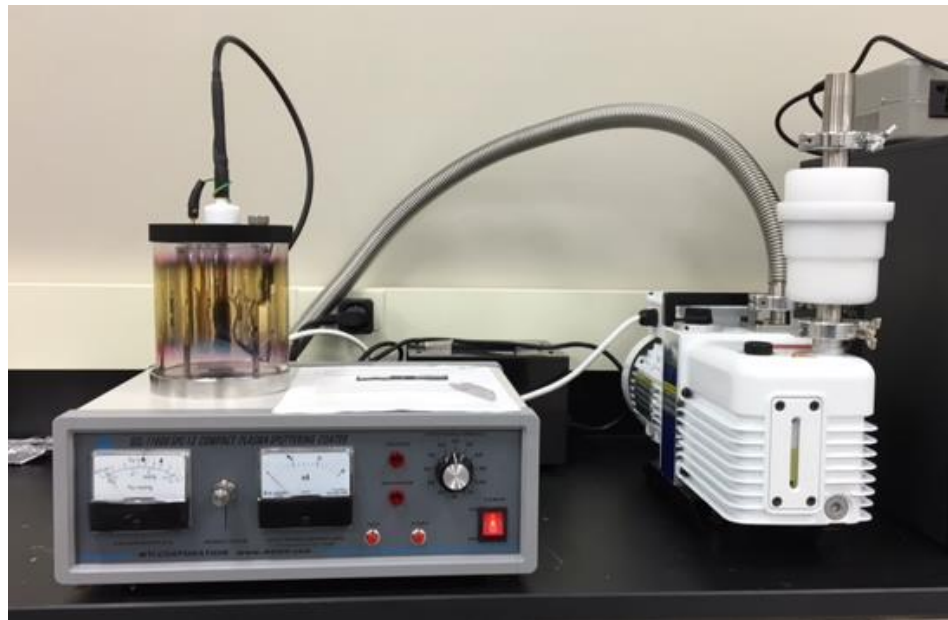


Figure 32: MTI Corporation model GSL-1100X-SPC12-LD sputter coating machine located in Marquette University Dental Research Laboratory

To begin the sputtering process, the sample is lightly rubbed with a 1200 grit sand paper. The sand paper on the surface allows the light reflecting to be in a cone shape. Prior to rubbing the surface with sandpaper, the surface was a smooth surface and it was

extremely difficult to get adequate light return into the PDV collimator. When the surface was smooth, the light was reflecting as a single beam that at times was angled away from the collimator's face depending on alignment. The rough surface on the PMMA plate coated with gold creates a cone shaped reflection so more light is absorbed into the PDV. After rubbing the surface, a stencil is cut out of paper in the shape of a circle to coat the PMMA just in the center. This past step is an optional step. Next, the sample is loaded into the sputter coating machine and the lid is placed on the machine. The machine is turned on and a vacuum is pulled. Once the vacuum is pulled, a button labeled 'test' is pressed to check the number of mA the machine will run at. It is ideal to run the machine around 10 mA, if the value is higher the PMMA could melt in the machine from the heat. If the number is too low, it will take longer to achieve the desired thickness of gold to sputter. If the test is greater or less than 10mA, the pressure is adjusted until 10 mA is achieved. The timer on the machine is set to one minute and then the 'run' button is pressed. At the end of one minute, the vacuum stays pulled and two minutes is waited until the next minute of sputtering begins. A break between sputtering is required because without the break, the PMMA might melt or the gold could bubble on the surface of the PMMA. For this experiment, two minutes of sputtering was found to be the optimal amount of time to sputter based on experimental trial and error. Two minutes of sputtering results in 10 nm thickness of gold on the surface of the PMMA plate. This number was acquired from Figure 33:

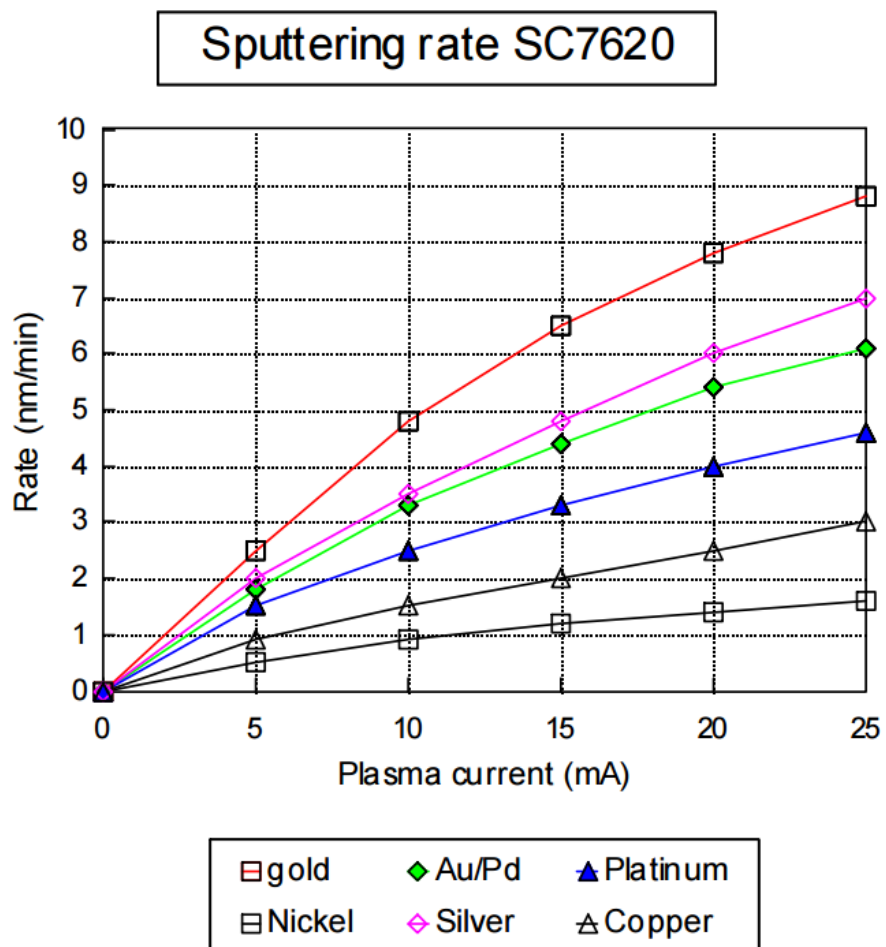


Figure 33: Graph for determining thickness of the gold sputter coating [18].

Figure 34 shows an example of a back anvil disc post sputtering.

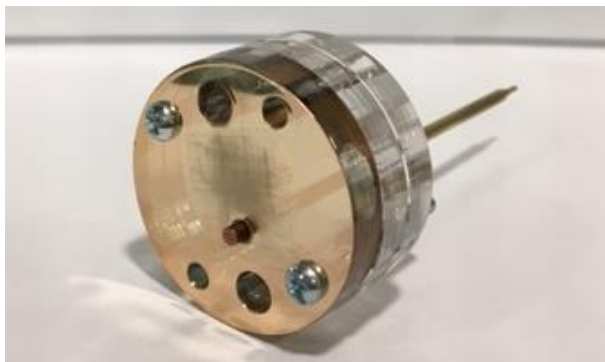


Figure 34: A sample after being sputter coated for two minutes.

4.4 Target Design Validation

The target design was validated using a Hydrocode named CTH developed by Sandia National Laboratories [27]. The code simulations were performed by Jeff Lajeunesse at Marquette University. The goal of the validation was to ensure the shock front completely passed through the water sample prior to rarefaction waves interfering with the experiment. In Figure 35, the flyer, traveling perpendicular to the x-axis, comes into contact with the driver at 0 cm on the y-axis. The water sample is contained between the driver and the flyer, represented by the blue rectangle in Figure 35. The simulation was run for 5 microseconds with data output every 0.05 microsecond. Figures 36-49 represent the pressure wave below.

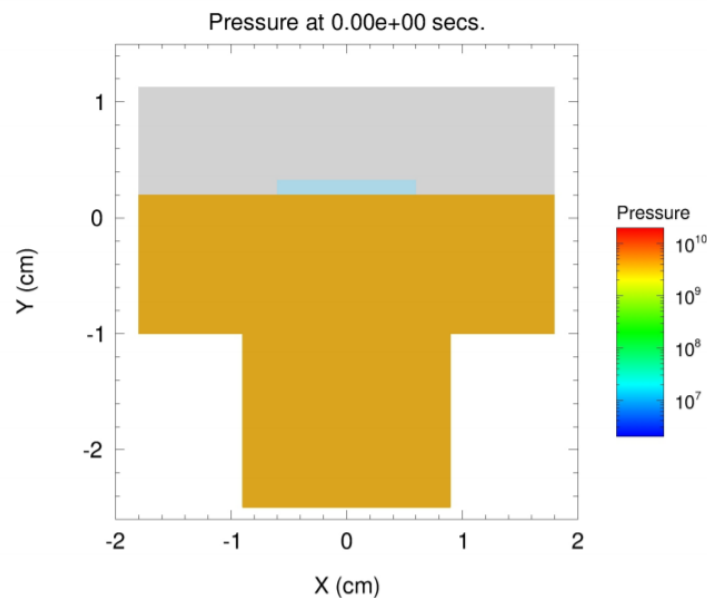


Figure 35: Hydrocode set up

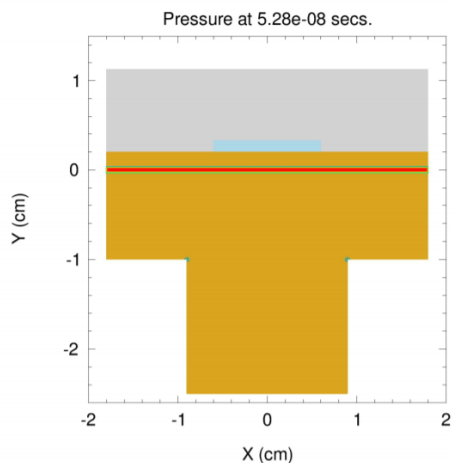


Figure 36: Pressure wave propagating at $5.28e-8$ seconds

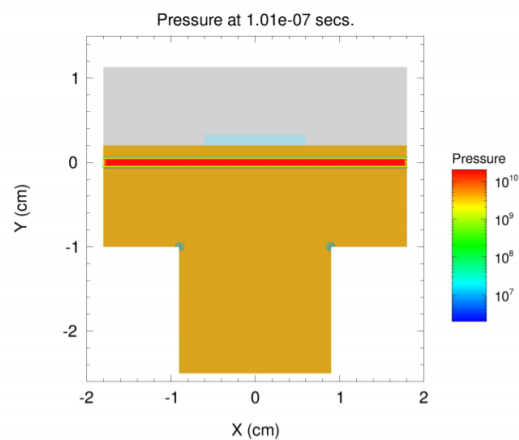


Figure 37: Pressure wave propagating at $1.01e-7$ seconds

The shock wave begins to propagate through the material represented by the red line in Figure 36 where the flyer and driver come into contact. In Figure 37, one can see the rarefaction wave that is formed from the impact.

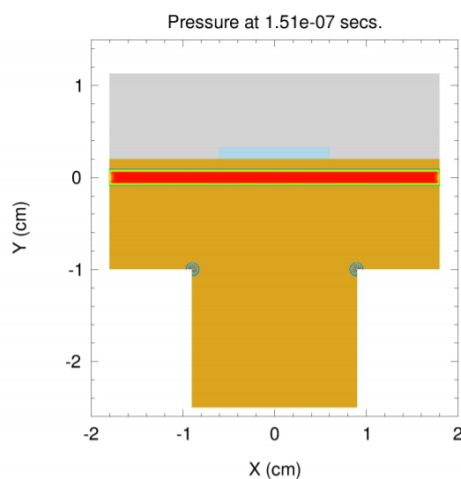


Figure 38: Pressure wave propagating at $1.51e-7$ seconds

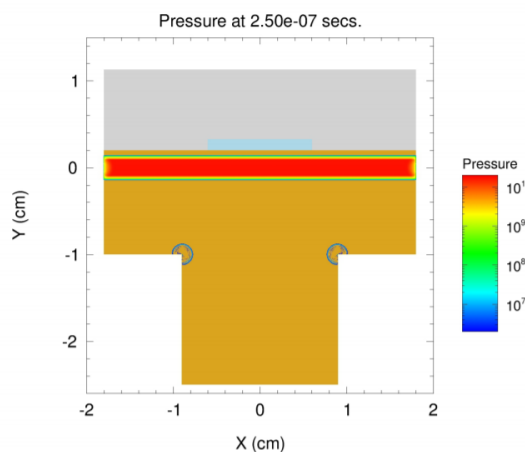


Figure 39: Pressure wave propagating at $2.50e-7$ seconds

Figure 38 and Figure 39 begin to show the propagation of waves in the corners of the flyer that are caused from the stress of the impact.

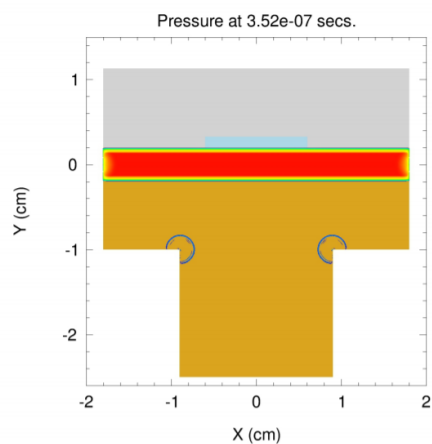


Figure 40: Pressure wave propagating at $3.52e-7$ seconds

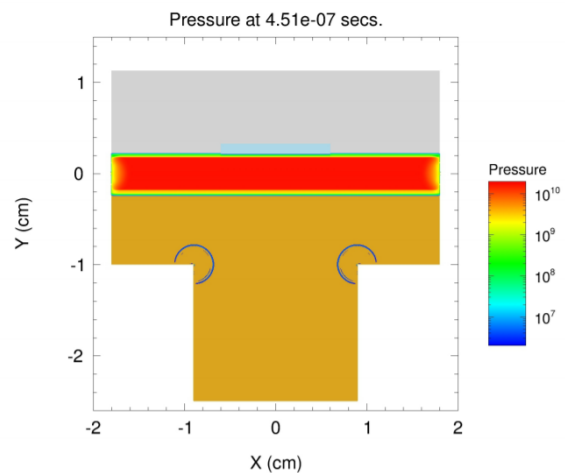


Figure 41: Pressure wave propagating at $4.51e-7$ seconds

In Figure 40, the shock front reaches the water sample and rarefaction waves begin to form on the side walls of the target. The goal of this is to ensure the waves from the sides of the target do not interact with the shock front passing through the water sample.

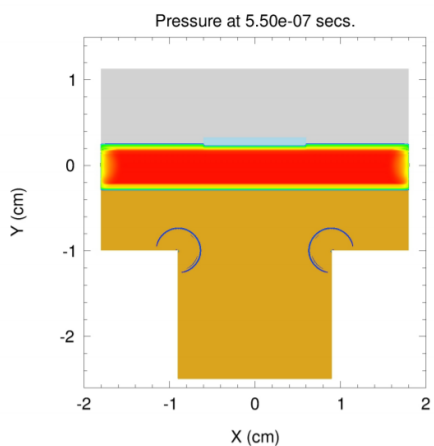


Figure 42: Pressure wave propagating at $5.50e-7$ seconds

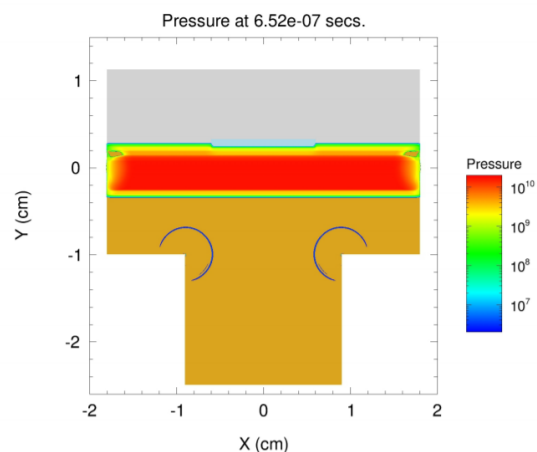


Figure 43: Pressure wave propagating at $6.52e-7$ seconds

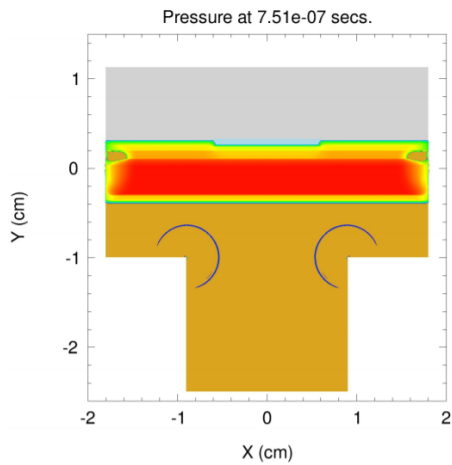


Figure 44: Pressure wave propagating at $7.51e-7$ seconds

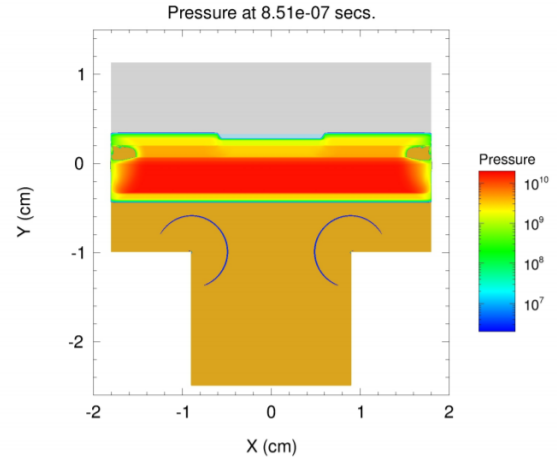


Figure 45: Pressure wave propagating at $8.51e-7$ seconds

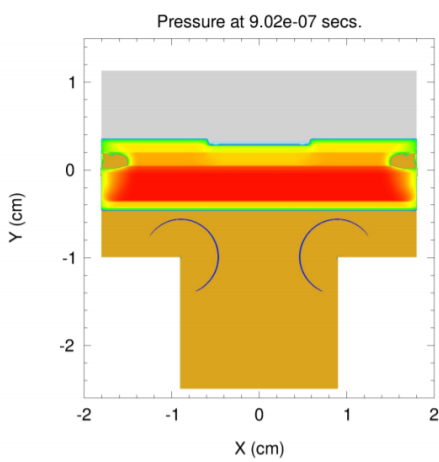


Figure 46: Pressure wave propagating at $9.02e-7$ seconds

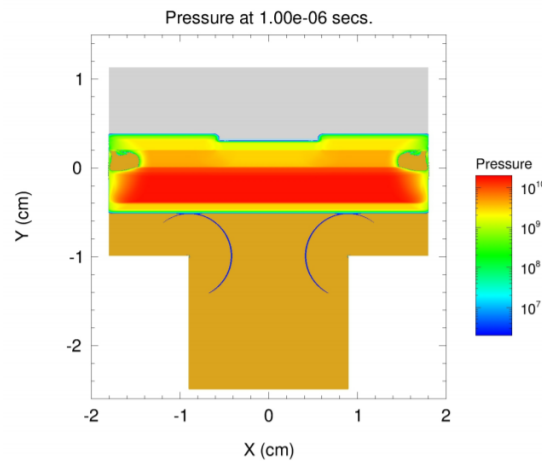


Figure 47: Pressure wave propagating at $1.00e-6$ seconds

In Figures 41-47, the wave continues to travel through the water sample and the rarefaction waves creep closer to the centerline of the water but still have not reached the centerline.

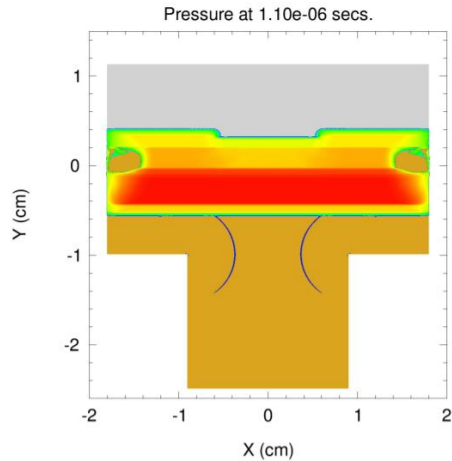


Figure 48: Pressure wave propagating at 1.10e-6 seconds

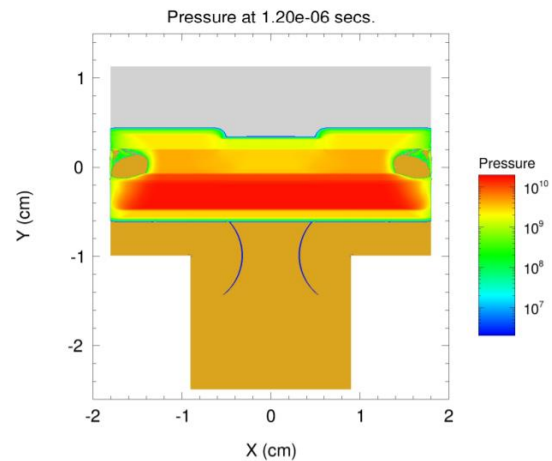


Figure 49: Pressure wave propagating at 1.20e-6 seconds

In Figure 48 and Figure 49, the shock front completely passes through the water and the experiment is completed. Based on this simulation, the target design has been validated. The shock front passes through the water sample prior to rarefaction waves interfering with the data collection. From these simulations, it can also be expected that the experiment will conclude in less than 1.2 microseconds.

4.5 Target Assembly Process

Before a target was assembled, all of the necessary parts were made in the Discovery Learning Center at Marquette University. Once the parts were made, the faces of the back anvil G plates were sanded lightly with 1200 grit sandpaper. Next, the back anvil G plates were taken to the Marquette University Dental Research Laboratory and sputtered with gold for two minutes with the MTI Corporation model GSL-1100X-SPC12-LD sputter coating machine. After sputtering, the target is ready for assembly. Each target was assembled individually to ensure no mistakes were made.

To start the target assembly process, a PZT pin is soldered to a stripped BNC cable. The positive end of the BNC cable was soldered to the smaller diameter of the PZT pin and the ground on the cable was soldered to the larger diameter of the PZT pin. After soldering the PZT pin, the PDV laser system is turned on to allow the lasers to warm to a desired wave lengths of the target and reference lasers. Using a PZT pin for alignment, two back anvil plates are first super glued together with Loctite Super Glue. Next, the back anvil plate that was gold sputtered was super glued to the other two plates with Loctite Super Glue and the gold side facing out. This glue is allowed to set for 15 minutes. After fifteen minutes, the water housing plate and front anvil are screwed to the back anvil plates with four 2" #4 screws. The PZT pin is placed through its channel and pushed lightly against the driver plate. Loctite Super Glue is used around the base of the PZT pin to hold it in place permanently. While this glue is drying, two o-rings are placed on the sabot and the flyer is inserted into the sabot. Next, vacuum grease is spread on the outside of the sabot and the sabot is inserted into the gun's barrel. The gun is now loaded and caution should be used if testing the pressure system of the gun. After loading the sabot, a Mylar burst disc is cut into to the outer diameter of the barrel. Vacuum grease is placed on the outer diameter of the Mylar burst disc and the disc is placed in the opening of the barrel behind the projectile. At this point, the breach of the gun is pulled to the barrel and the two ends are bolted together using a crescent wrench. At this point, the glue holding the PZT pin in place should be dry. If the glue is dry, the driver plate is removed from the assembly. A sewing needle is used to spread a minimal amount of super glue around the base of the PZT pin from the inside of the water housing. This step

insures the water will not leak down the PZT pin chamber. This glue is allowed to set while the oscilloscopes settings are checked.

The oscilloscope for the PZT pin is first checked by assigning the desired settings and putting a BNC cable into the device with banana plug ends. The oscilloscope is set to trigger and a Duracell A, 1.5 V, battery is touched to the positive and negative banana clip. If the scope triggers when introduced to the battery voltage then it is ready to use. Next, a ten foot BNC cable is attached to the trigger out of the PZT oscilloscope and strung to the trigger in channel of the PDV oscilloscope. The desired settings are put into the PDV oscilloscope and it is set to trigger. The trigger with the 1.5 V battery is checked again on the PZT oscilloscope. At this point, both of the scopes should trigger when introduced to the battery. If this does not occur, the settings are checked and tested again.

At this point, the target is ready to be filled with water. Using a clean 50 ml beaker, water is acquired from the drinking fountain in Engineering Hall at Marquette University. All six plates are now screwed together with four #4 2" screws. The nuts are left loose by 5 mm so the micropipette can fit in-between the water housing plate and the driver plate. Water is injected into the water housing and the plates are pushed together and held tight. The nuts are hand tightened and then further tightened with a Philips head screw driver and wrench.

Next, the target is mounted to the target plate with two #6 2" screws and tightened down. Following this, the velocity pins are laid in place in the stripper box and the lid is put in place. Next, the third and final oscilloscope should be checked before lowering the target plate to be aligned with the barrel. To check the scope, a trigger is set to channel 2

and the BNC cable in channel 2 should be removed. If channel 2's line on the screen has a downward slope, then the velocity pins are correctly in place and properly working. The target plate is now lowered to be aligned with the barrel and a protective lid is put over the target plate and stripper box.

A PDV collimator can now be inserted into the target in the proper channel to the left of the PZT pin. The collimator is aligned with target light until the optical power meter (Eigen lights) read between -20 and -10 dbm. Once the eigen lights read this value, the collimator is glued in place using Loctite Super Glue.

After an hour of letting the PDV collimators glue dry, a protective cap is placed over the target and mounts to the target plate. This catches all of the debris and stops the projectile after passing through the target. After the cap is bolted into place, the experiment is ready to be conducted.

When conducting the experiment, the three oscilloscopes are all set to trigger immediately when signal is reached. Next, the PDV lasers are turned on and the target and reference lasers are attenuated. Next, the operators put on hearing protection and go up range from the gun. The tank is pressurized to around 500 psi and then the burst disc ruptures. Once the burst disc ruptures, the flyer moves and strikes the target. Once this happens, the air and lasers are immediately turned off. At this point, it is safe to move up range of the gun. The data from all three oscilloscopes is saved to a USB drive and transferred to a computer. These steps are repeated for each experiment with very little variation.

5. Diagnostics

5.1 Pressure Measurement Design

A pressure measurement system has been installed onto the small gas gun to remotely control and monitor the pressure. This was completed as a safety precaution for the gas gun operator. A Dwyer Pressure Transducer Model #628 S37846402 has been installed to the back end of the breech. The transducer is rated for up to 5000 psi. While most shots will be well below 600 psi for this study, the small gas gun is rated up to 5000 psi for future experiments. The pressure transducer requires a small (3inch x 2inch) LCD screen for the reading output. The LCD screen is a Dwyer DPMA-401, and can numerically display up to 999.9 kpsi. The LCD screen and pressure transducer require two power sources. The power source supplies approximately 20 volts to the back light of the screen. The LCD screen is located 20 feet away from the gun behind a protective shield for the operator and observers. An air hose utilizing shop air is connected to the breach, and extends from the gun to the operator area. In the operator area, one can control the amount of air flow while being protected and watching the LCD screen to see the amount of pressure in the breach. 50 shows the LCD screen and nozzle that controls pressure in the gun.



Figure 50: Dwyer DPMA-401 LCD screen with a pressure control valve.

As a backup method for determining the pressure in case the LCD screen is not functioning properly, there is a pressure gage installed on the gas gun. The pressure gage is made by Swagelok and is rated up to 2000psi. The pressure gage is attached to the gun and has two needles. The red needle shows the maximum pressure that was obtained and the black needle shows the current pressure in psi. Figure 51 below shows the Swagelok gage and Dwyer pressure transducer.

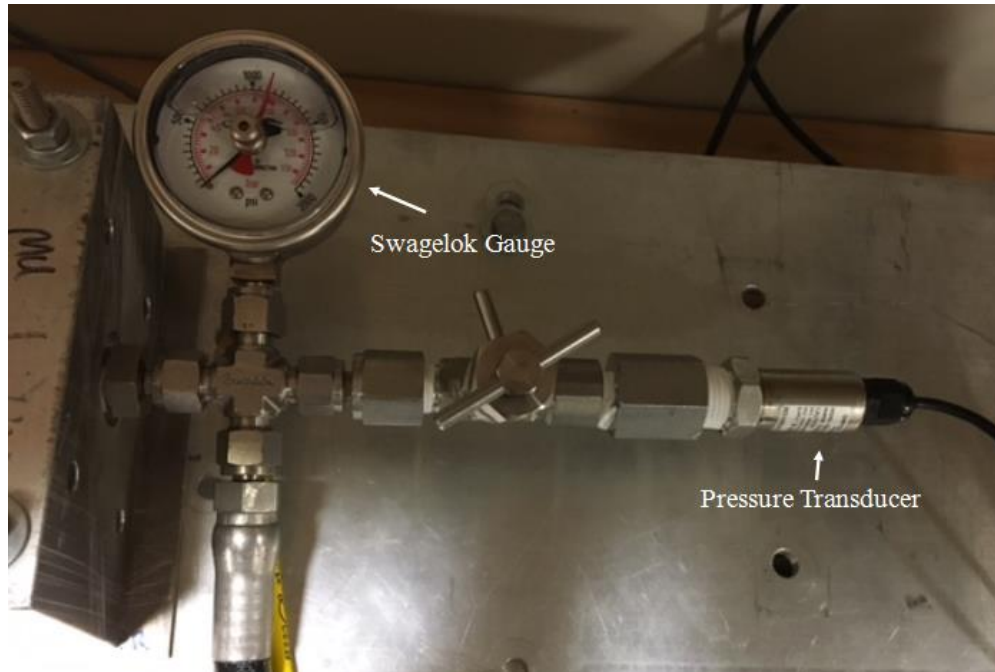


Figure 51: Swagelok gage and Dwyer pressure transducer

5.2 Velocity Pins

A break pin system is incorporated into the small gas gun. Graphite pins, four in total, are housed in a circuit located in the stripper box. The stripper box is located between the target plate and barrel. When the flyer leaves the barrel, it encounters the graphite break pins. When the break pins are broken, the circuit is opened, and the signal is then read by an Agilent Technologies DOS-X-3034A oscilloscope. The scope is set to a falling edge trigger of 250 mV. Each channel triggers when the circuit is opened. The spacing between each break pin is known and the oscilloscope outputs the time at which each pin was broken. Using Equation 30 described below, the flyers velocity is able to be obtained. Figure 52 shows the oscilloscope output after an experiment was conducted.

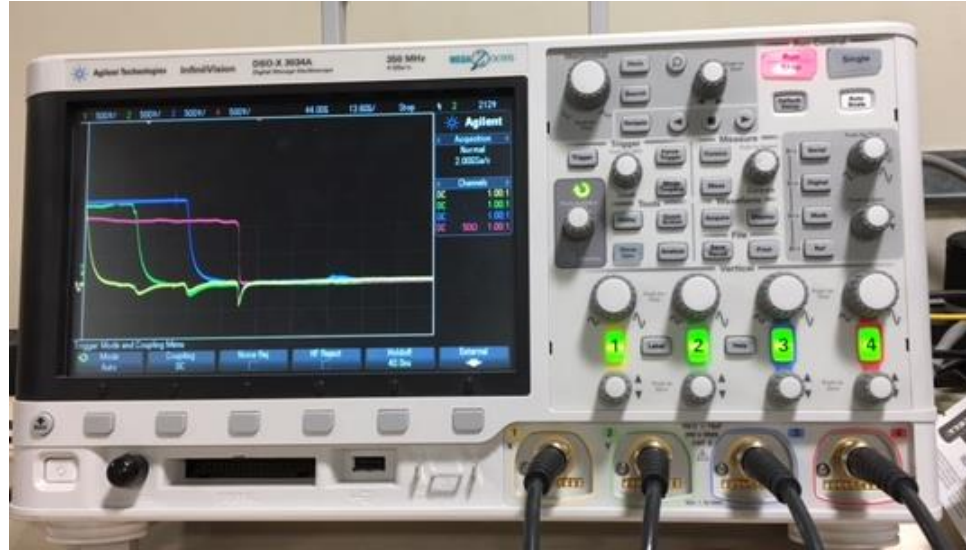


Figure 52: Agilent Technologies DOS-X-3034A oscilloscope with an output from velocity break pins

5.3 Piezoelectric Pin

A piezoelectric pin (PZT pin) is a position sensor that outputs a signal when the shock front arrives to the surface. The PZT pins are supplied by Dynasen, Inc. located in California. The CA-1136 PZT is composed of a 0.093 inch brass outer diameter. Inside the brass housing is a 0.020-inch thick PZT-5A crystal. When a stress is induced, the crystal outputs a voltage that is read by an oscilloscope. These pins are able to function from as little as a few psi up to 300 kbar of pressure. The scope requires a 50 ohm terminator connected to a BNC cable before connecting to an oscilloscope. The pin has a 10 nanosecond response time when the cables are less than 1m. The pin outputs up to 70 volts for 0.5 microseconds. For pressures below 2kbar, the output is near linear [28].



Figure 53: Piezoelectric Pin [19]

Special cables are available for use when connecting the PZT pin to an oscilloscope. These cables have a BNC end and are insulated. For this experiment, normal BNC cables were acquired and one end was stripped. Next, the 0.093 inch diameter portion of the pin is prepped for soldering by applying Bernzomatic water soluble flux onto the pin and wires of a one sided BNC cable, and soldered using Kester #66 lead solder see Figure 54 . The back end of the pin has a smaller diameter, and is attached to the positive portion of a BNC cable with solder, see Figure 55. Soldering wire to the PZT pin yields the same results as using the special cables from Dynasen Inc., but simply cost less and can be reused. After each shot, the BNC cables can be stripped again and reused until the cable is either too damaged or too short for experimental constraints.



Figure 54: Soldering set up for connecting a BNC cable to a PZT pin.

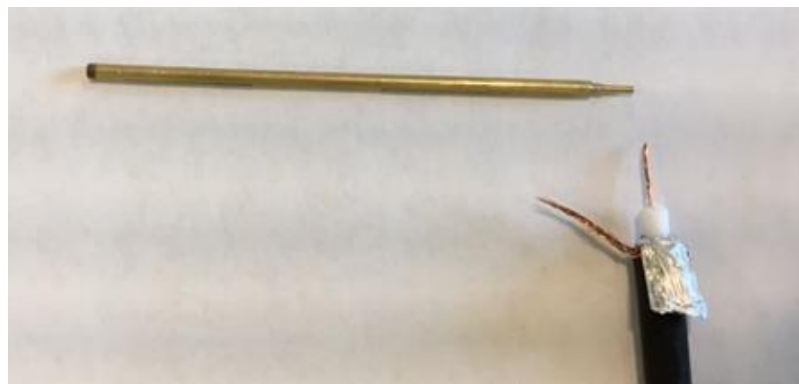


Figure 55: BNC cable aligned to a PZT pin.

To measure voltage from the pin, a Tektronix DPO 4032 Digital Phosphor Oscilloscope was used. The BNC cable carrying the voltage from the PZT pin went into a

T-connector located on the designated PZT oscilloscope. Proceeding from the T-connector was a 75 ohm terminator. The PZT oscilloscope was triggered off of source 1 when a 500 mV signal occurred. The trigger was DC coupled with a rising edge. The PZT oscilloscope was also utilized as a trigger out to the oscilloscope being used for PDV.

5.4 Photon Doppler Velocimeter

Photon Doppler Velocimetry (PDV), combines Doppler shifted light with an unshifted light source to determine the velocity of a dynamic target. PDV works by emitting 1550 nm light incident on a target, and collecting a portion of return light. When a dynamic target is subjected to emitted target light, this light is then Doppler shifted. The Doppler shifted light is then combined with light contained within the system, and outputted to an oscilloscope. There are two types of PDV systems: homodyne and heterodyne. Homodyne functionality uses only one wavelength, where the shifted light and unshifted light came from the same source. A heterodyne system, however, has two light sources that are variable frequency. The PDV located in the Shock Physics Lab at Marquette University is a heterodyne system. The laser that will be Doppler shifted is known as the target laser, and the non-shifted laser is known as the reference laser. The reference laser is contained within the system at all times, and is not Doppler shifted. The target light, however, is Doppler shifted when incident on a dynamic target. When the shift occurs, the light is directed back into the PDV and then combined with the reference light. The difference between the two frequencies, known as the beat frequency, can be resolved as a result of the combination of the two light sources. This signal can be processed using a Fast Fourier Transform (FFT) to determine beat frequency, and can be

used to calculate the velocity of the dynamic system. This system is demonstrated in Figure 56.

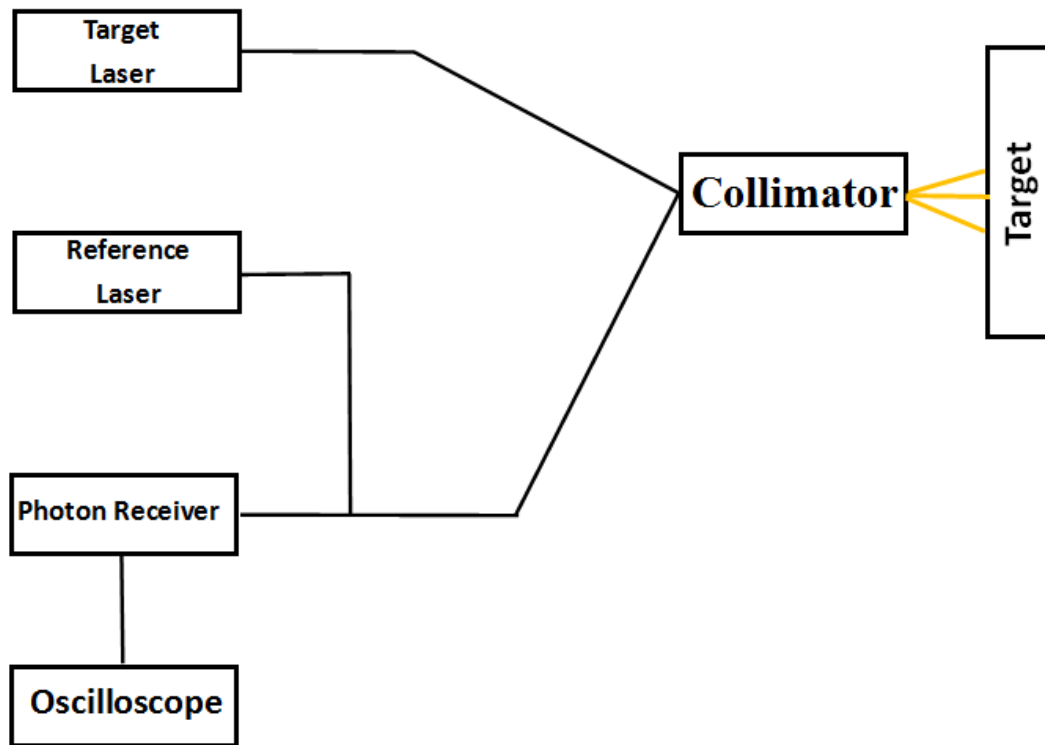


Figure 56: Schematic of the Photon Doppler velocimeter (PDV) at Marquette University.

To calculate the velocity of the dynamic target, an Agilent Technologies DSO9404A Digital Storage Oscilloscope was set to collect frequency data beginning when the PZT oscilloscope sent the trigger. The oscilloscope was set to take 41 million data points at a rate of 20 gigasamples per second. This scope continued to collect data with a rising edge until the storage of 41 million data points is full. When performing data analysis, there is a definite change in frequency. This shift in frequency represents

the Doppler shifted light seen at the back of the sample, and represents the shock wave velocity through the sample. The data represents the point when the wave is known to have reached the back surface of the water sample. These key pieces of information allow for shock velocity to be calculated.

5.5 Data Analysis

A series of seven coding scripts are run consecutively to process each experimental shot. Matlab 2016b and Maple 2016 are both used as each program has their own specific benefits. The goal of these seven scripts is to determine the shock and particle velocity to create a plot and then curve fit a Hugoniot line to the data. Each script described below is attached in the appendix of this document.

Script #1 and 2

The initial flyer velocity must be determined from data outputted by an oscilloscope connected to velocity break pins (See Chapter 5.2). This combines a function file with a script file. Data is retrieved from an oscilloscope connected to the break pins. The script computes the center point of the falling edge data to find the time that each pin was broken. To find the velocity between pin 1 and 2, Equation 30 is used.

$$V_{12} = \frac{dx}{t_2 - t_1} \quad (30)$$

Both times for Equation 30 are determined from Figure 57 and dx is the spacing between each break pin, 0.00655 m. The velocity between pins 2 and 3 and 1 and 2 are found. Taking the sum and averaging the three velocities outputs the initial flyer velocity.

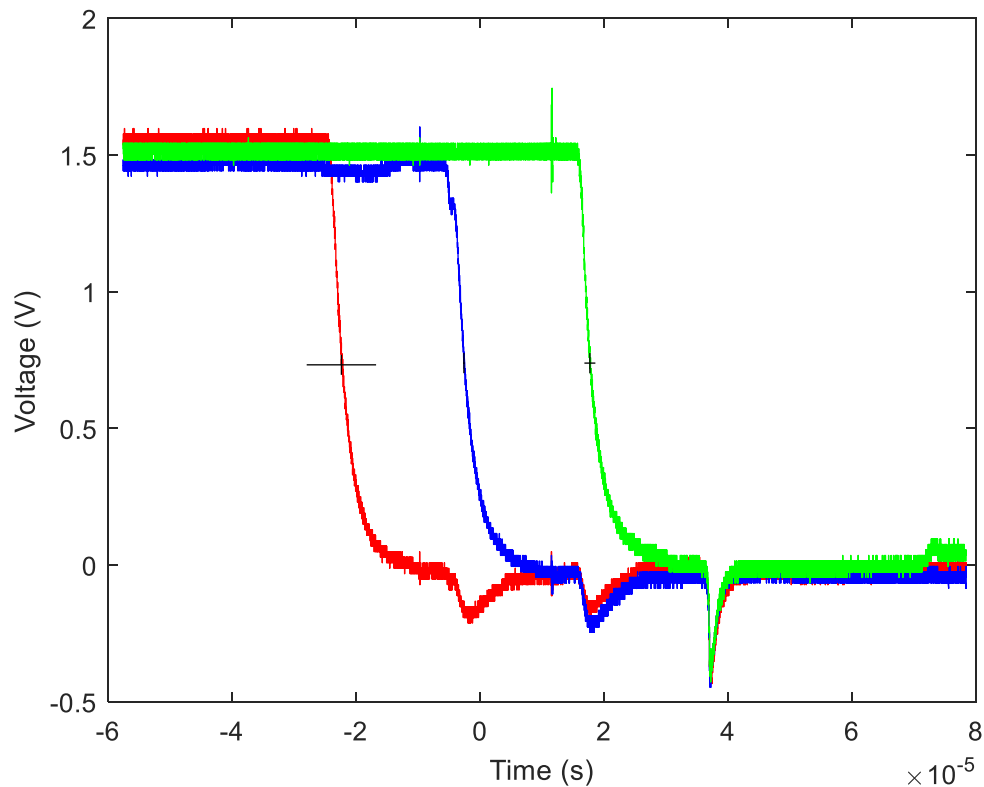


Figure 57: Time versus Voltage output from the break pin oscilloscope

Script #3

To begin, the data from the oscilloscope connected to the PDV is loaded into Matlab 2016b script to run a Fast Fourier Transform. A Fast Fourier Transform (FFT) converts the data from the time domain into the frequency domain. An FFT must be computed on a 2^N basis [29]. For this analysis, N was chosen as 25 which results in 33554432 data points being studied. N cannot be 26 because the maximum data points available from the oscilloscope is 41 million and 2^{26} is larger than 41 million. To shift from the time to frequency domain, the code shifts windows from the left to right of the data. Within the windows, the data points is further broken down until a median point is

found. A minimal window size is preferred while still ensuring a good resolution of the data occurs. For this research, the window size was set to $0.08e-5$ seconds. Each window contained 2,003 data point and each window was set to overlap to gather the most accurate findings.

The 41 million data points begins to retrieve data when the flyer impacts the front surface of the water. A PZT pin (See Chapter 5.3) is located at the front surface of the water and sends a 70 volts signal to an oscilloscope when impacted. The PZT scope sends a trigger out to the PDV oscilloscope and data begins to be recorded instantaneously

The code used to process this data initially graphs all 41 million data points as an amplitude versus time basis (Figure 58).

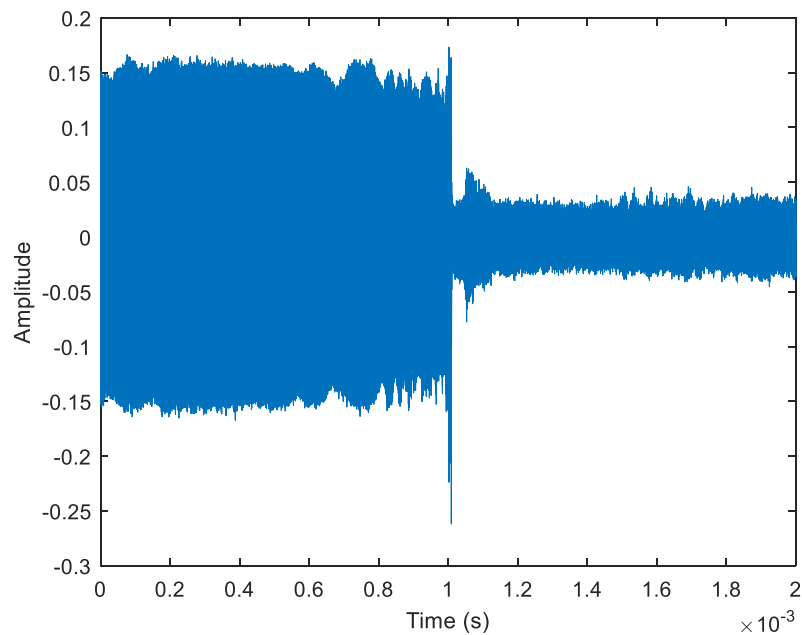


Figure 58: Time versus Amplitude graph of the complete set of data.

Next, the code performs an FFT early in the data to find the beat frequency of the experiment. Figure 59, is an example of an FFT taken early in the data.

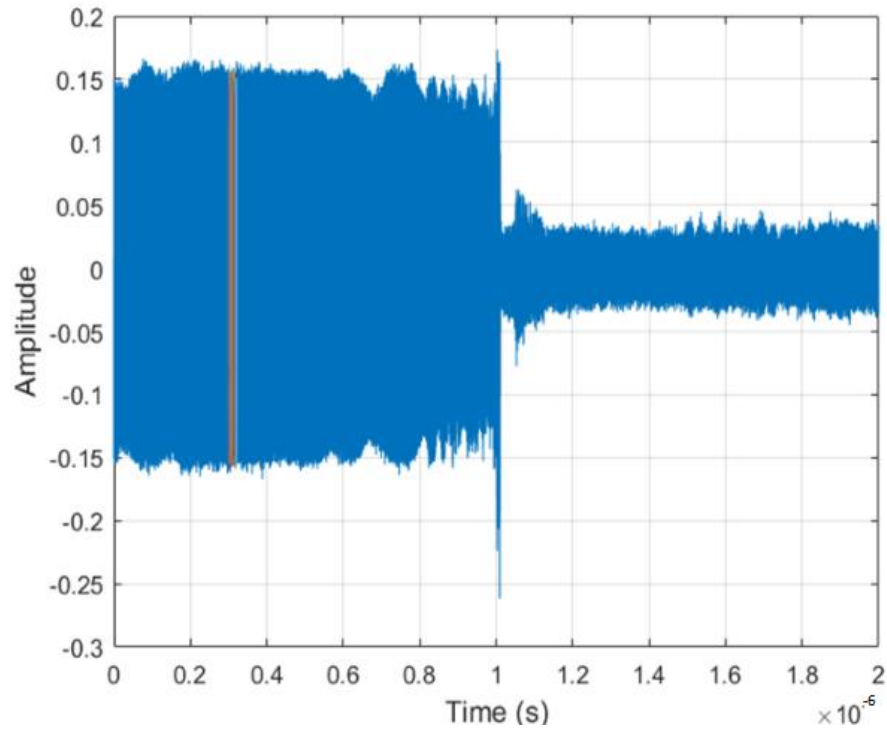


Figure 59: Time versus Amplitude graph with an FFT performed in the early section of the data.

The colored sliver in the graph is where the FFT was performed. Figure 60, shows a zoomed in portion of the data to demonstrate the shifting of the FFT windows from left to right.

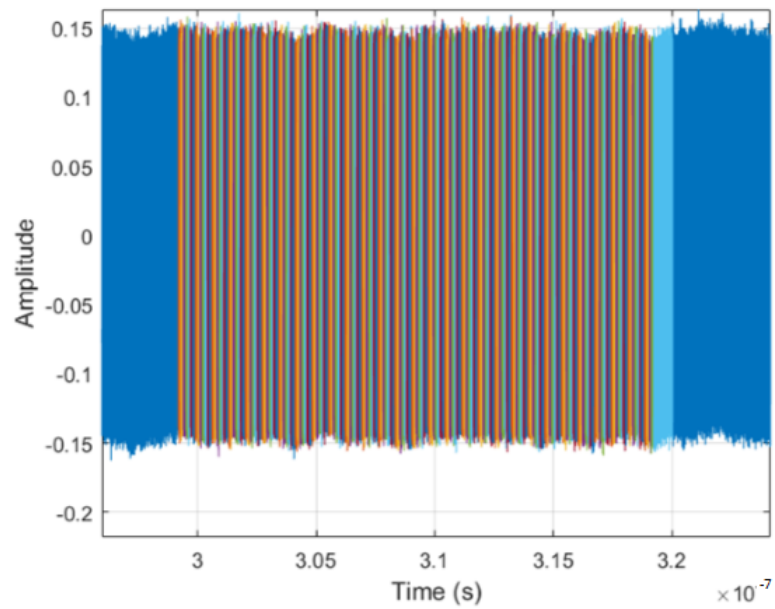


Figure 60: Time versus Amplitude graph with a zoomed in portion of the FFT window.

The time in Figure 60 is converted into a frequency via the FFT. As the amplitude versus time graph processes, a graph of amplitude versus frequency is processed simultaneously. This graph is how the beat frequency is determined (Figure 61). While the PDV displays the target and reference laser wavelengths, there is error associated so the beat frequency is gathered from the data for more accuracy.

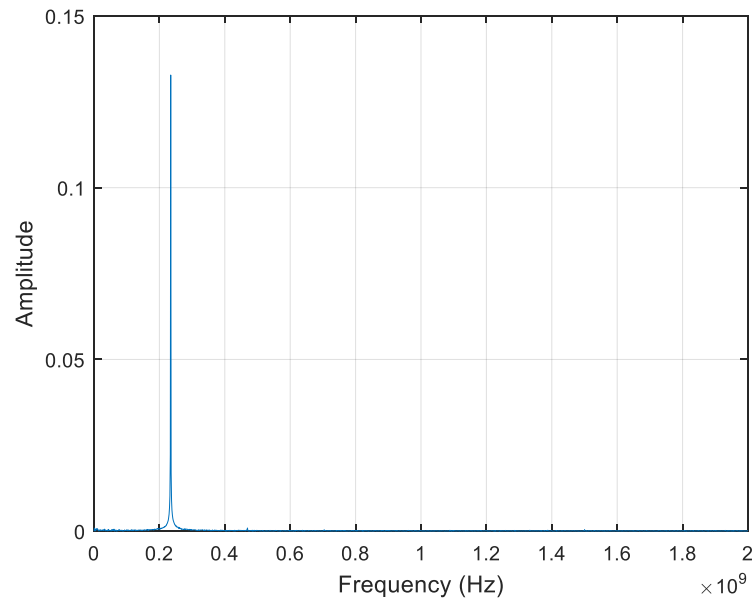


Figure 61: Frequency versus Amplitude for a single FFT sample window.

To determine the beat frequency, the graph is zoomed in to find the center of the peak on the x-axis. This value is then inputted into the same MATLAB script file and an FFT is performed where a shift in frequency is detected. Figure 61 demonstrates this past step.

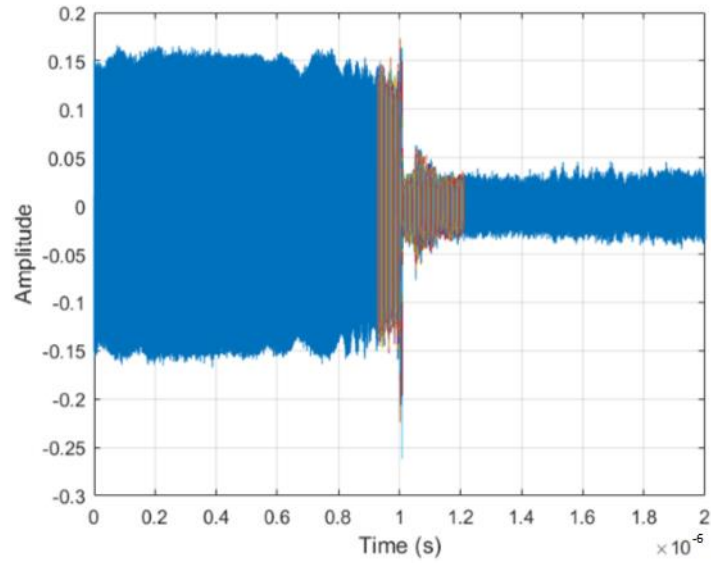


Figure 62: Time versus Amplitude of the frequency data with an FFT performed.

After this step, a contour plot is created showing the frequency versus time. This graph shows when a shift in frequency is detected. This shift in frequency represents when the shock front reached the back surface of the water sample in the target. Figure 63 is an example of a contour plot.

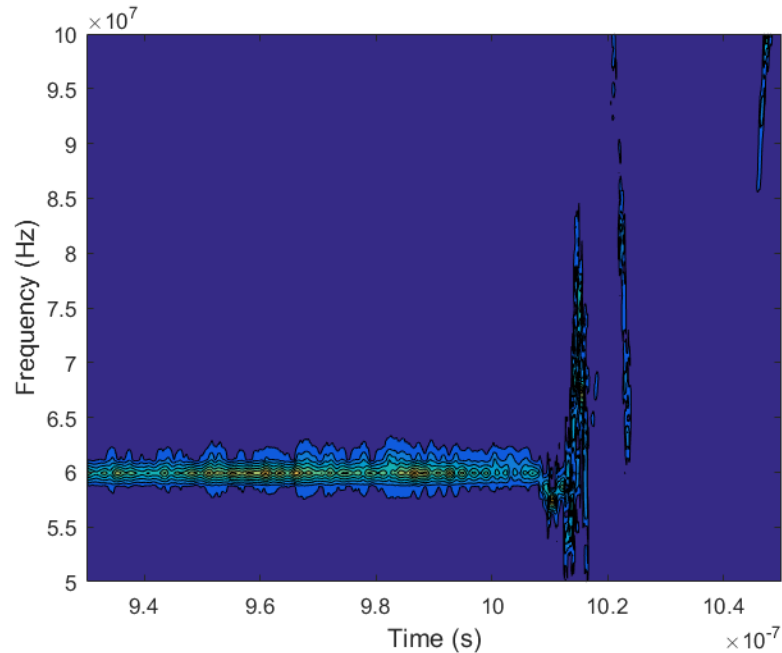


Figure 63: Contour plot of time versus frequency

Figure 63 clearly shows a shift in frequency around 1.01×10^{-6} seconds. So for this particular experiment, the change in time for the wave to reach the front of the water sample to the back of the water sample is 1.01×10^{-6} seconds. This time value is inputted into a script in Maple 2016 to begin impedance matching.

Script #4

The goal of the fourth script is to determine the shock velocity and particle velocity values for a set of data. To do this, the initial flyer velocity and change in time from Script #1/2 and Script #3 is inputted into Script #4. The necessary bulk sound speed, density, and slopes of each material are entered into the designated constant field. Following the impedance matching procedure from Chapter 3.6, the particle velocity from Equation 12 and Equation 13 is computed with a graph that visually demonstrates

the results. In this example, the flyer and driver are copper. Depending on the flyer and driver materials, the slope of the graph in Figure 64 would change.

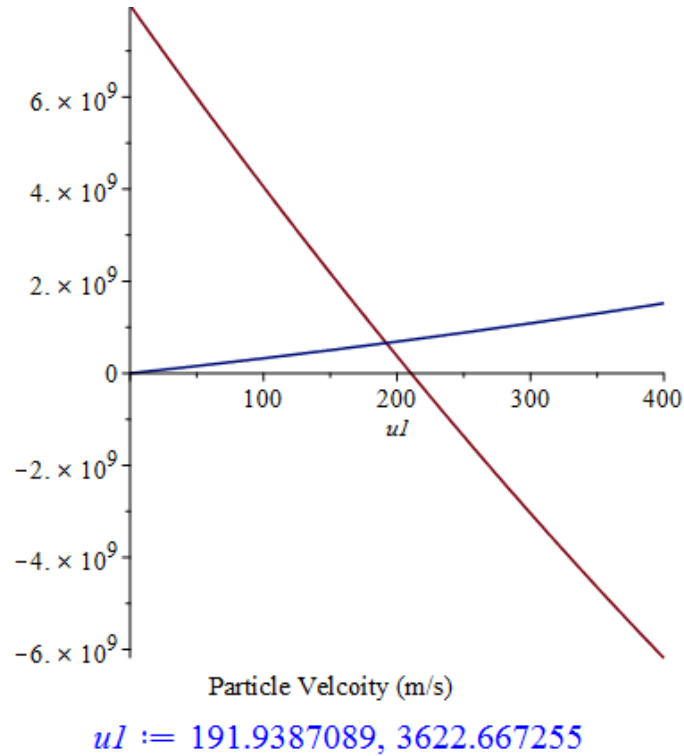


Figure 64: Particle Velocity versus Pressure for the flyer and driver interface.

In Figure 64, the red line is the left going rarefaction wave and the blue line is the right going shock wave. Two particle velocity (U_1) data values are shown because the equation (Equation 17) to find the value is a quadratic. The smaller of the two U_1 values is inputted into the script to solve for the particle velocity (U_p) of the water sample using

Equation 21 and Equation 22 from Chapter 3.6. Figure 65 graphically demonstrates the output.

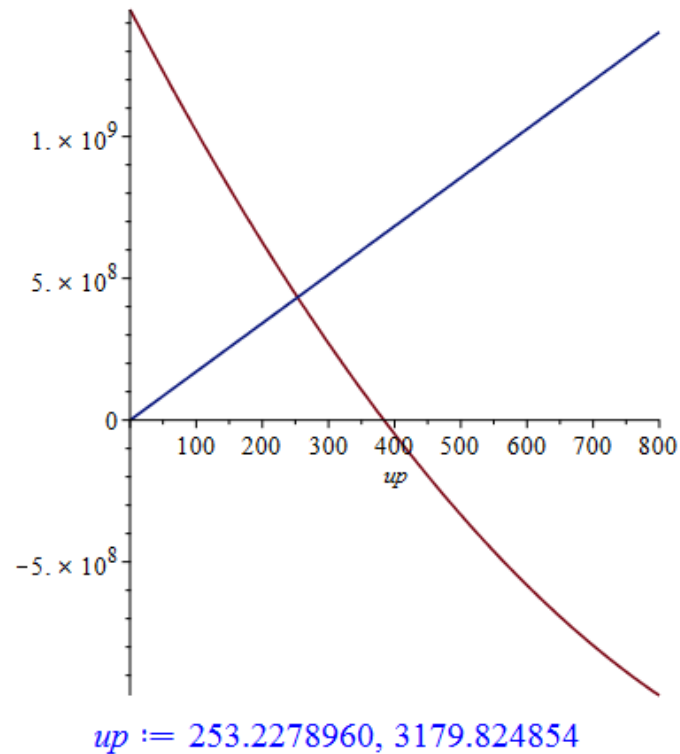


Figure 65: Particle Velocity versus Pressure for the driver and water interface.

In Figure 65, the red line is the rarefaction wave traveling through plate B and the blue line is the shock wave traveling through the water sample. The first Up value is the particle velocity of the water sample. This value is now taken and placed into Script #5 in Matlab. From the graph in Figure 65, the shock pressure can be determined by tracing a line from the left and right going Hugoniot's intersection points to the y-axis. The y-axis is the shock pressure in Pa.

Script #5

The fifth script is a collection of the shock and particle velocity data points for each experiment that was completed. This script, written in Matlab, makes a scatter plot of particle velocity versus shock velocity. Once all of the data points are collected, the collection of data points is curve fitted with a first order polynomial in the curve fitting application in Matlab. The curve fitting tool will output an equation with the necessary constants to form a Hugoniot line (Equation 29). Error bars can be fitted to the data points by calculating them with an additional script.

Script #6

Uncertainty analysis is completed in Maple for finding the shock velocity and particle velocity [30]. Each portion of finding the error in the calculations is considered. As an example, the error analysis for finding the shock velocity is demonstrated below. Shock velocity is a function of distance (x) and time (t) showing in Equation 31.

$$U_s = \frac{x}{t} \quad (31)$$

Equation 32 is used to calculate the error.

$$\partial U_s = \sqrt{\frac{\partial U_s(x, t)}{\partial x} \partial x^2 + \frac{\partial U_s(x, t)}{\partial t} \partial t^2} \quad (32)$$

The uncertainty in the constants for the error calculations is $\pm 5\%$ of the known value. All other uncertainty values are from measurement uncertainty. This process was completed for each equation used to solve for the particle velocity in a similar approach to the method shown in Equation 32. Once the uncertainty is known for both the shock

and particle velocity, the values can be stored in Script #5 and placed on the Up vs. Us graph.

6. Results and Discussion

An experiment was designed in Chapter 4 to launch a projectile into a stationary water target. The experiment, conducted in the Shock Physics Laboratory at Marquette University, aimed to characterize the shock structure of water in the low-pressure region (>1 GPa). The experiment created one-dimensional and steady shock waves in water through a flat plate impact. The flat plate or flyer, made of copper, aluminum, or PMMA ranged in velocities from 200 m/s to 350 m/s. The flyer struck a stationary water sample enclosed in a PMMA housing. The front driver of the housing was aluminum, PMMA, or copper depending on the test run. Data was recorded in oscilloscopes from break pins, a PZT pin and a PDV collimator which outputted to three oscilloscopes. The data was analyzed in MATLAB and Maple using the methods described in Chapter 5.

In the current section, the results will be presented, analyzed and compared to published data as well as data from a Hydrocode performed by Jeff Lajunesse of Marquette University. Once the experimental results are presented they will be presented with error analysis.

Six experiments were completed using the small gas gun with a 12.7 mm bore at Marquette University. The flyer, driver, and Mylar burst disc combinations are shown in Table 1. Varying the combinations allowed for higher particle velocities to occur due to the impedances of the materials and the pressure limits of the Mylar burst discs. The combinations were chosen based on simulations completed in Maple. These simulations aimed to predict the shock and particle velocity to give a variation in the results.

Table 1: Flyer, driver, and Mylar burst disc combinations for each experiment

Experiment Number	Flyer Material	Driver Material	Number of Mylar Burst Discs
1	PMMA	PMMA	1
2	PMMA	PMMA	1
3	Copper	PMMA	1
4	Aluminum	Aluminum	1
5	Copper	Copper	1
6	Copper	PMMA	2

To begin, the experimental results were calculated using MATLAB and Maple along with the calculations described in Chapter 3. The following table of variable constants were used in the calculations when necessary [22].

Table 2: Variable constants used to calculate the theoretical results of the experiment at Marquette University.

	Density (g/m ³)	Bulk Sound Speed (m/sec)	s
Copper	8930	3940	1.489
PMMA	1186	2598	1.516
Aluminum	2785	5328	1.338

The process of impedance matching was used to calculate the particle velocities at the driver-water interface. Table 3 presents the results of the results of the experimental values which were calculated using Matlab and Maple.

Table 3: Experimental results of the small gas gun experiment conducted at Marquette University

Experiment Number	Flyer Material	Driver Material	Flyer Velocity U_0 (m/s)	Particle Velocity in Driver U_1 (m/s)	Particle Velocity in Water U_p (m/s)	Shock Velocity U_s (m/s)
1	PMMA	PMMA	328.22	164.11	215.92	1685.07
2	PMMA	PMMA	316.77	158.39	208.28	1710.09
3	Copper	PMMA	210.15	191.94	251.54	1714.34
4	Aluminum	Aluminum	259.67	129.57	232.43	1720.32
5	Copper	Copper	211.67	106.08	202.00	1693.33
6	Copper	PMMA	327.19	297.02	396.27	1718.61

Experimental results show variation in shock velocities, ranging from around 1685 m/s to 1720 m/s. Particle velocity also exhibits a separation in velocities, spanning between 202 and 396 m/s. An interesting comparison can be made between the shock and particle velocity. The range of shock velocities is 35 m/s, while the range for particle velocities is 194 m/s.

The shock velocity and particle velocity were plotted to find the Hugoniot line in Figure 66. To find the Hugoniot line, the curve fitting tool in Matlab was used to calculate the slope and y intercept values. The equation of the line in Figure 66 is shown in Equation 33.

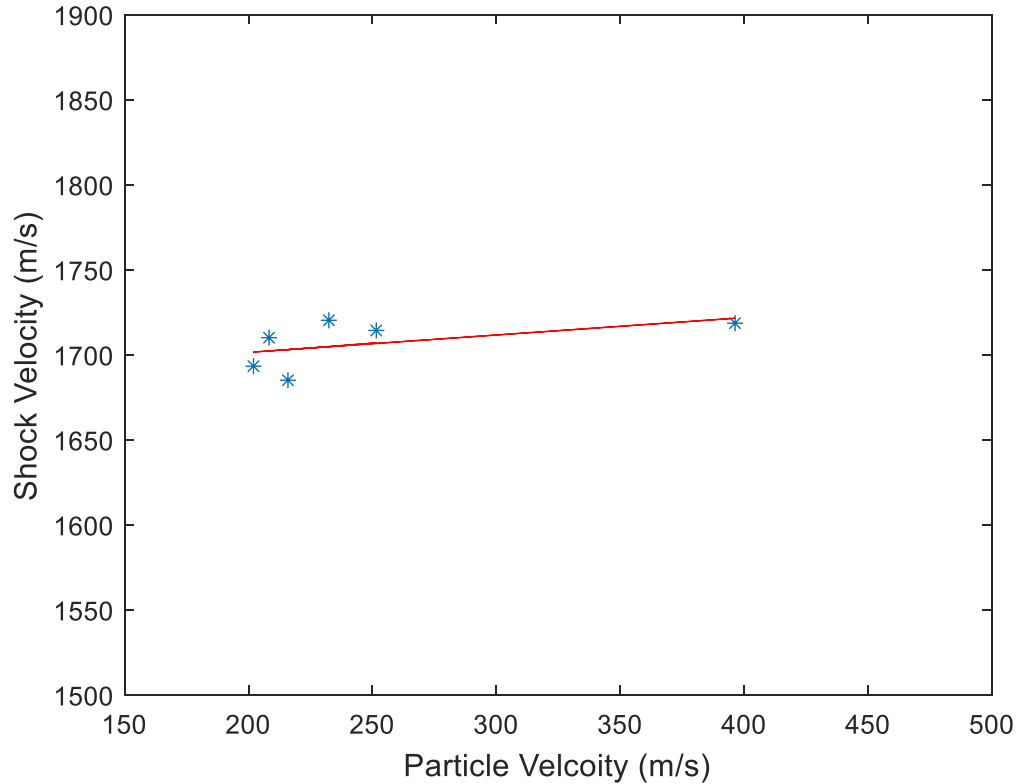


Figure 66: Experimental Results of the small gas gun experiment conducted at Marquette University.

$$U_s = 0.1022U_p + 1681 \quad (33)$$

The experimental results were studied at pressures much less than 1 GPa compared to other experimentalist who were able to achieve higher shock pressures. Table 4 shows the shock pressure obtained in the experiment conducted at Marquette University. The average shock pressure obtained was 0.45 GPa. The shock pressure was determined from impedance matching and finding where the left going and right going Hugoniot intersect. Knowing the shock pressure allows for other thermodynamics properties to be calculate such as temperature and entropy.

Table 4: Experimental pressure values.

Experiment Number	Flyer Material	Driver Material	Pressure (Gpa)
1	PMMA	PMMA	0.37
2	PMMA	PMMA	0.36
3	Copper	PMMA	0.51
4	Aluminum	Aluminum	0.40
5	Copper	Copper	0.35
6	Copper	PMMA	0.70

A Taylor Series of error, developed by the American Society of Mechanical Engineers (ASME), was computed in Maple on the experimental data [30]. For each constant the uncertainty of the constants would be $\pm 5\%$. For example, the bulk sound speed of copper is 3940 m/s so the uncertainty related to copper is ± 197 m/s. The error for the experimental results is tabulated in Table 5 and demonstrated on Figure 67. The red lines in Figure 67 are the error bars and the blue line is the Hugoniot.

Table 5: Experimental Uncertainty

Experiment Number	Flyer Material	Driver Material	Particle Velocity Error U_p (m/s)	Shock Velocity Error U_s (m/s)
1	PMMA	PMMA	10.85	82.19
2	PMMA	PMMA	10.41	84.65
3	Copper	PMMA	12.64	85.07
4	Aluminum	Aluminum	11.62	85.66
5	Copper	Copper	10.1	82.99
6	Copper	PMMA	19.86	85.49

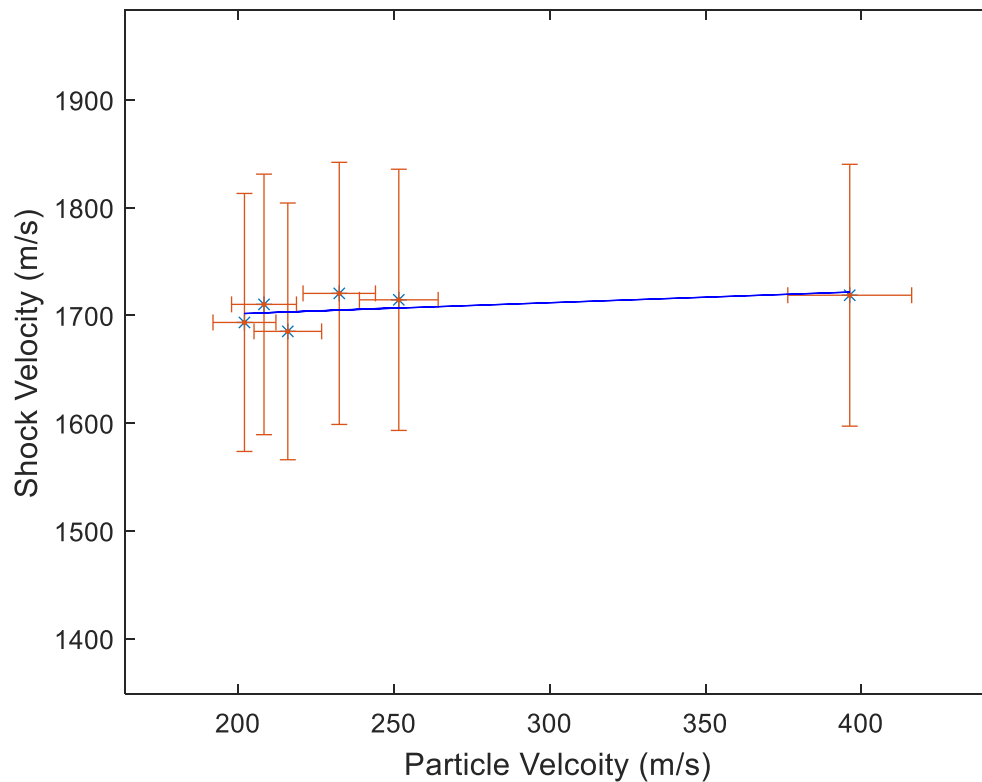


Figure 67: Experimental Results of the small gas gun experiment conducted at Marquette University presented with uncertainty analysis.

6.1 Comparison to Simulations

The experiment conducted at Marquette University was simulated in a Hydrocode developed by Sandia National Laboratories [5]. The simulations were conducted on the experimental setups listed in Table 1 and utilized the flyer velocities determined from the break pins. This was done in two parts: with the PZT pin integrated into the design and without the PZT pin in the design. An example of the output of the simulations is shown in Figure 68 for the design without the PZT pin. The graph shows two sharp rises on the particle velocity axis. The difference between the two rises on the time axis demonstrate the time the wave theoretically passed through the water sample.

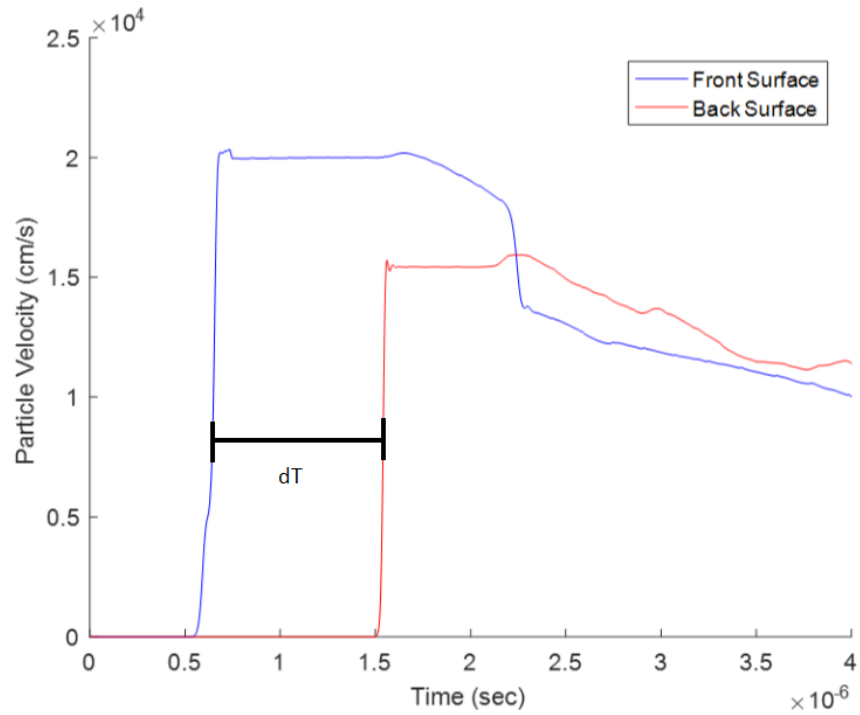


Figure 68: Simulated results used to find the wave traveling time.

The time difference is entered into the impedance matching code discussed in Chapter 3.6 to find the shock and particle velocity. The results of this are presented in Table 6.

Table 6: Experimental and simulated shock and particle velocity results.

Experiment Number	Experimental Particle Velocity Up (m/s)	Experimental Shock Velocity Us (m/s)	Simulated Particle Velocity w/ pin Up (m/s)	Simulated Shock Velocity w/ pin Us (m/s)	Simulated Particle Velocity w/o pin Up (m/s)	Simulated Shock Velocity w/o pin Us (m/s)
1	215.92	1685.07	207.06	1931.99	207.18	1928.75
2	208.28	1710.09	200.09	1920.09	200.20	1919.75
3	251.54	1714.34	239.29	2010.47	239.69	2003.94
4	232.43	1720.32	228.96	1976.07	229.87	1907.45
5	202.00	1693.33	199.37	2183.57	199.65	2130.65
6	396.27	1718.61	362.78	2228.93	362.89	2231.81

It is interesting to note the large difference between the experimental and simulated shock velocity values. Whereas the particle velocity values are near in value ranging by less than 20 m/s. Figure 69 shows the simulations and experimental results graphically compared to one another.

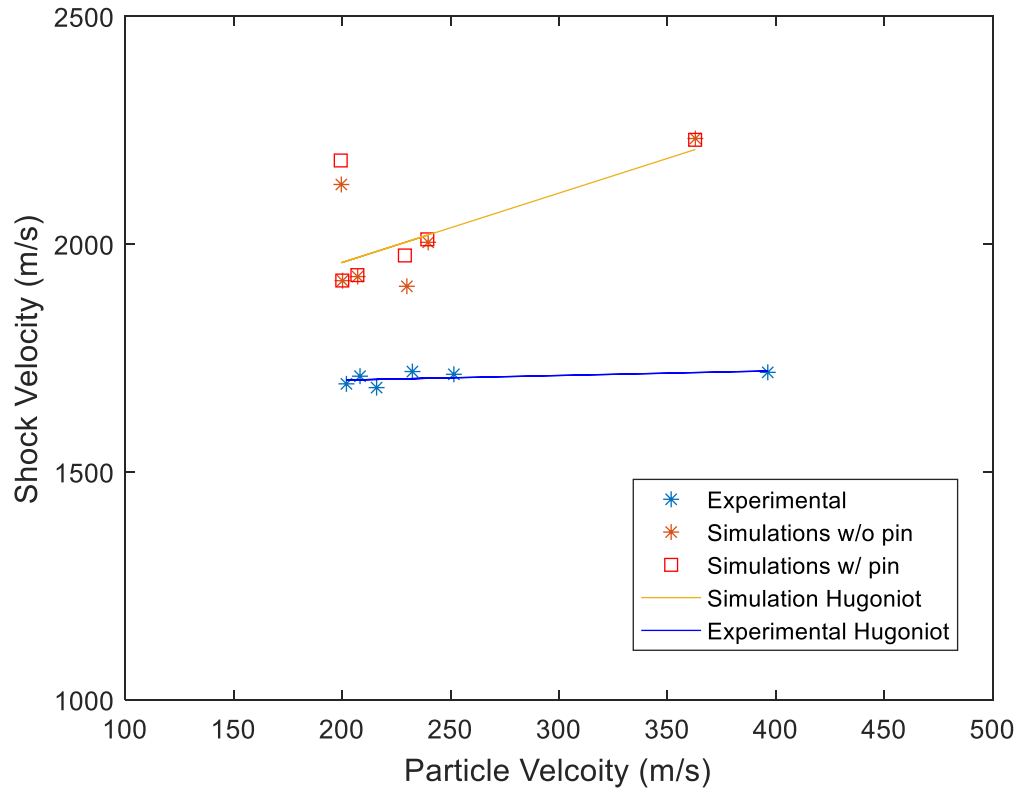


Figure 69: Experimental and simulated results.

The Hugoniot line related to the simulations was determined using the curve fitting application in Matlab; the result is presented in Equation 34.

$$U_s = 1.523U_p + 1655 \quad (34)$$

The bulk sound speed of the experimental and simulated Hugoniot differ by 26 m/s and the slope varies by 1.402. The bulk sound speed value of the simulated and experimental results are relatively close with only 1.5% difference, however the slope has a 93% difference. The difference in the slope is primarily dependent on the shock velocity, namely the change in time value used to calculate the shock velocity. To more clearly demonstrate the differences between the experimental and simulated data, Figure

70 presents the experimental results with the measurement uncertainty presented as error bars.

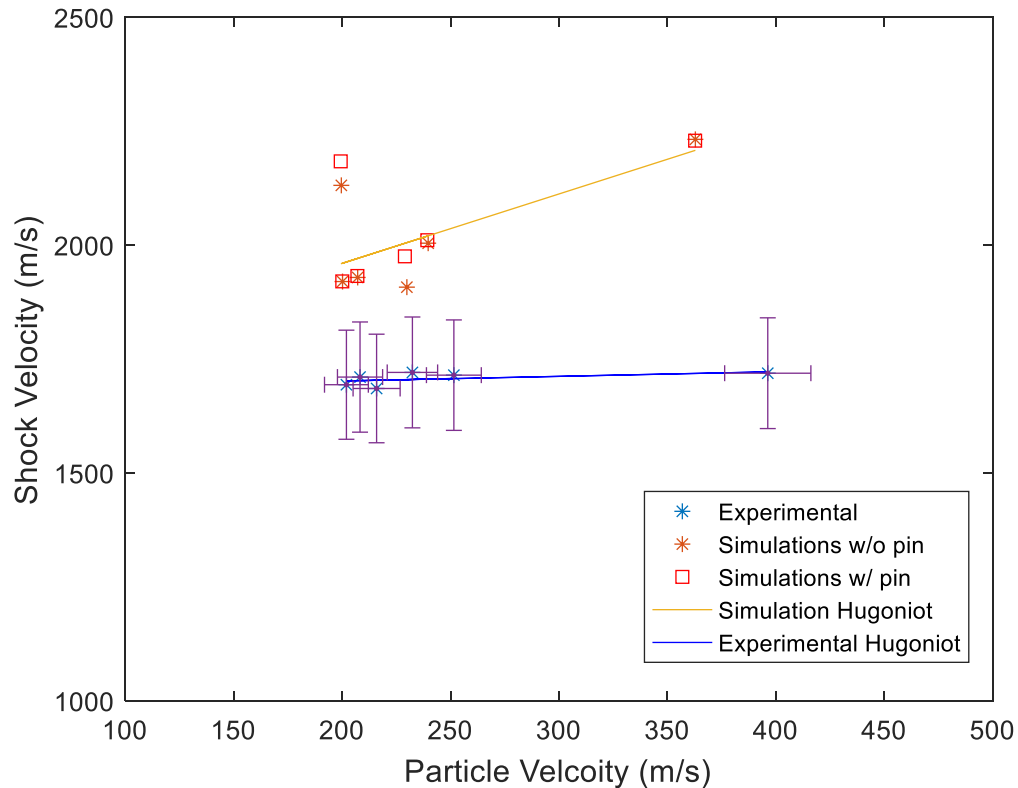


Figure 70: Experimental and simulated results displayed with error bars

There are many sources of experimental uncertainty and errors which include the equipment, measurement techniques and calculations. The uncertainty associated with the calculations is presented in Table 5 above and was tabulated from a Taylor Series Error Analysis method. It is interesting to note that the particle velocity values for the simulated and experimental results are near in value and range between than 10 m/s. However, the shock velocity values are ranging by more than 100 m/s. The shock velocity is dependent on the change in time from when the wave traveled from the front to back of the surface of the water and by the thickness of the water. The thickness of the

water remained constant through each experiment however the time difference did change. Determining the time that the shock wave traveled from the front to the back of the surface was dependent on the data recorded by a PZT pin and a PDV. Table 7 demonstrates the times associated with each experiment and the time difference between the simulated and experiment results. To find the time the wave was traveling experimentally, a contour plot showing frequency versus time was created from an FFT in Matlab (See Chapter 5.5). When the wave reached the back of the water surface, a clear change in frequency shifted in the graph. At this point, it was assumed the wave reached the back surface of the water and this was the change in time. Figure 63 demonstrates the shift in frequency to determine the change in time.

Table 7: Time difference between the simulated and experimental results for the waves travel time.

Experiment Number	Simulated w/o pin dT (microsec)	Simulated w pin dT (microsec)	Experimental dT (microsec)	Difference b/w Simulated and Experimental (microsec)
1	0.8955	0.894	1.025	0.131
2	0.8977	0.899	1.01	0.111
3	0.8619	0.859	1.008	0.149
4	0.9055	0.874	1.004	0.13
5	0.8105	0.791	1.02	0.229
6	0.7739	0.774	1.005	0.231

At low pressures, a PZT pin is not the most desirable method to trigger an oscilloscope to begin recording data. Prior to the arrival of the projectile, sporadic signals could have been induced from shock induced polarization from the water [4]. It is also possible that from the vibration of the gun during firing, a false trigger signal could have

fired incorrectly from the PZT pin. A PZT pin, when induced, outputs a 70 volt signal and the oscilloscope was set to trigger at 500 mV. The low voltage was chosen as a trigger to ensure the signal was not missed however it might have been set too low and could have caused more experimental error than benefit. If this occurred, an oscilloscope would have begun collecting data at the incorrect time and the change in time from when the wave reached the front to the back of the surface of the water would be incorrect.

A possible source of vibration occurred when the flyer left the stripper box and traveled through the stripper plate. As the projectile leaves the breach and travels to the target, the flyer is in free flight because the barrel no longer guides the projectile. The projectile comes into contact with the break pins and then travels through the stripper plate. The stripper plate is 6.40 mm thick and has tight tolerances between the flyer diameter and the plates hole diameter. After the stripper plate, the projectile travels through the flat plate which is 6.38 mm thick and then makes contact with the target. If the flyer was no longer flying parallel to the floor while in free flight and clipped the target plate or the flat plate, this vibration could have traveled into the target and may have prematurely sent a signal to the scope. Doing an example analysis on the first experiment which had a flyer velocity of 328 m/s and a simulated and experimental wave propagation time of 0.894 and 1.025 microseconds. The change in time between the wave time is 0.131 microseconds. This change in time represents 0.0429 mm of flight distance. So if the projectile, which is 10 mm in head length, clipped the stripper plate or even the flat plate, that vibration could have induced the PZT pin to false trigger 0.131 microseconds prematurely.

After a few experiments, shavings from the flyer material could be found left in the stripper box. Also, after observing the projectile post shot, each projectile has scrapped lines running down the side of one side of the head. So it is possible to believe the interaction between the flyer and stripper plate contributes to the change in time of less than 0.20 microseconds between the simulated and experimental results.

If the shock transit time is incorrect, the shock velocity and particle velocity calculations would not be more closely related to the simulated and published results. An additional factor that would lead one to believe this is the outputted graph from the oscilloscope that recorded signal from the PZT pin. The graph was more of a bell shaped curve that quickly goes flat rather than a sharp rising edge (Figure 71). The signal should have been read by the oscilloscope and there should have been a sharp rise from the impact.

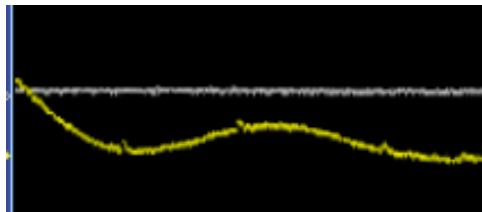


Figure 71: PZT pin oscilloscope output

In addition to the PZT pins sending an early false trigger to the scope, the PZT pin took up a considerable volume of the water sample as the pin was placed through the sample. The total volume of water was 215 mm^3 and the volume of the PZT pin in the water was 7.45 mm^3 . The pin also introduced spurious waves and while they did not interfere with the center of the shock front, they still interacted with the edges of the shock front. This interaction would cause the water sample to be at the Hugoniot state for

a shorter period of time. The length of time the sample is at the Hugoniot state can be seen in Figure 72 and Figure 73, at the point where the curves plateau.

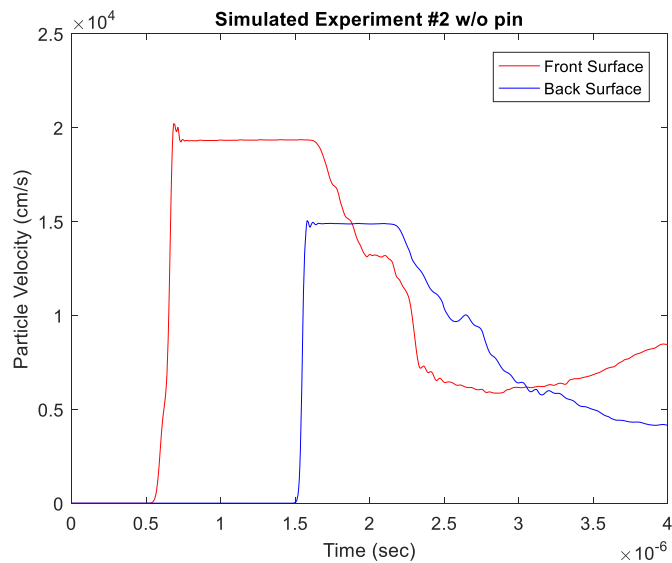


Figure 72: Simulated Results without a PZT pin in the design.

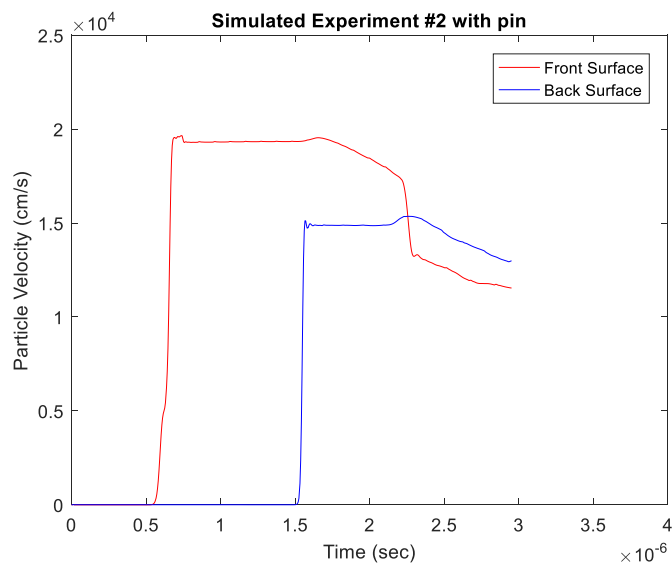


Figure 73: Simulated Results with a PZT pin in the design.

One can see the data presented including the PZT pin in the design (Figure 73) has a shorter plateau than the graph without the PZT pin (Figure 72). For the second experiment that was conducted, the simulations without a pin was at a Hugoniot state for 0.8674 microseconds and 0.7861 microseconds when the pin was simulated. The difference between the two states is 0.813 microseconds and the values were taken off of the graph in Matlab. Considering the experiment is concluded in less than 1.5 microseconds, this is a large change in time.

While using a PZT pin in the design that takes up volume in the water sample, this was the equipment selected and in retrospect may have affected the data. This leads to the limitations of the experimental setup. The experiment conducted at Marquette University utilized a small gas gun with a 12.7 mm bore. The limitations on the design based on the bore size caused significant data acquisition restraints. The thickness of the water sample had to be thin given the small bore of the gun. If the water sample was too thick, then a relief wave would interfere with the shock front. If a relief wave and shock front combine, they form a Mach Wave which would change the direction of the shock front. Having a thicker sample would have alleviated the need for a PZT pin on the front surface of the water. Instead, a high speed streak camera could have documented the shock front passing through the sample. This is similar to the experimental methods proposed by Cook and Mori [15] [2]. However, significant changes would have needed to be done to the gun to be able to incorporate a high speed camera which includes a larger diameter bore.

In addition to the bore size of the small gas gun at Marquette University, as the gun is pressurized and fired, the gun is not completely stationary. The gun is mounted to

a table which can vibrate and cause noise in the data recorded by the oscilloscope. This could have caused inaccurate values when doing the experimental analysis. The flyer diameter also had tight tolerances when traveling through the target plate. A larger diameter of the target plates hole would have allowed the flyer to not clip the plate while traveling through it.

To obtain velocity values, a PDV was used to collect data on the back surface of the water sample. The PDV has the potential to have a wandering wavelength overtime which in turn can affect the reading of the beat frequency. If the beat frequency reading is inaccurate, this could have a minor effect on the shock velocity value. Shock velocity is dependent on time and the thickness of the water sample. The thickness of the water sample has a controlled thickness with an uncertainty of ± 0.0005 mm. If the beat frequency is inaccurate, this will cause the time, shock velocity and in turn particle velocity to be inaccurate. However, this is believed to be a minor issue.

Further experimental error will be discussed below while comparing the experimental results to published data.

6.2 Comparison to Published Data

The data obtained from the experiment conducted at Marquette University is graphically displayed on Figure 74 and compared to six other experiments which were published by various authors [15] [16] [4] [2] [17] [31]. Each experiment utilized different methods which are described in Chapter 2.1. With the exception of Lynse [16], all of the experiments were conducted with pure distilled water.

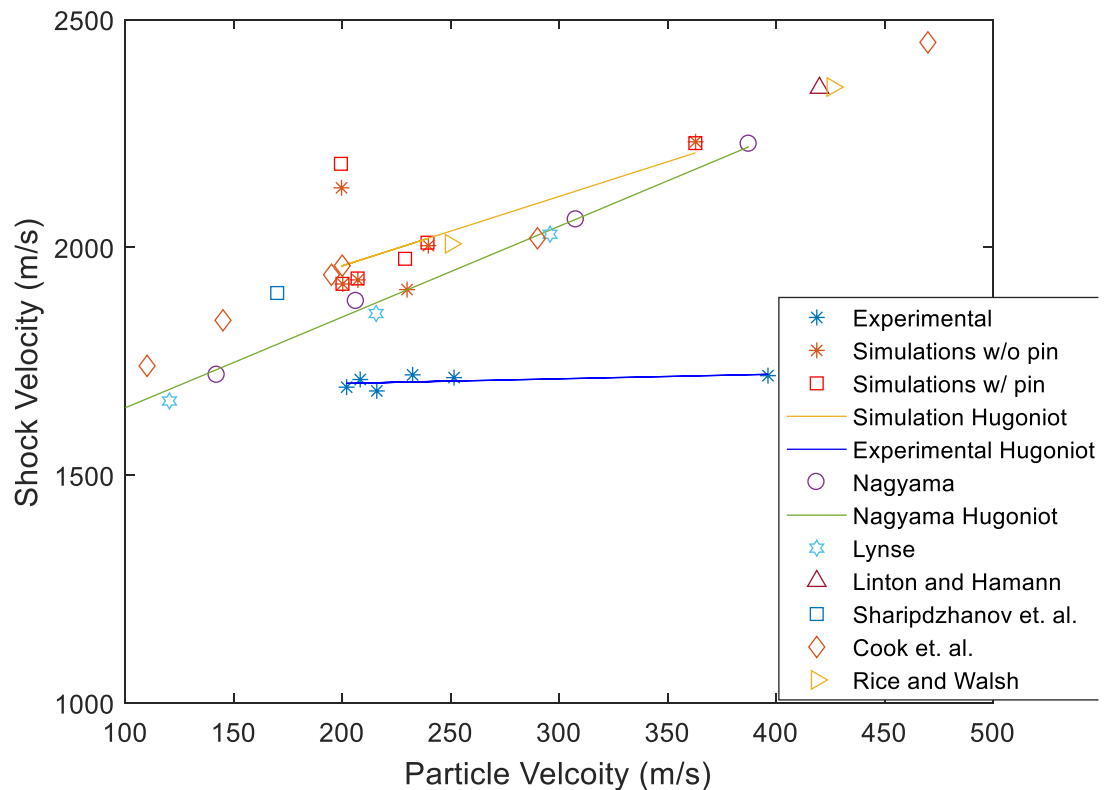


Figure 74: Experimental Results of the small gas gun experiment conducted at Marquette University compared to published data.

Figure 74 represents the published data of from six experiments and the results from these studies are presented. The green line represents the Hugoniot created from a study published by Nagayama et. al. In an article published by Nagayama, he stated that

the published data that is below 2 GPa has a large variation [4]. The data published in the Figure 74 above is all below 1.5 GPa and the experimental data is below 0.70 GPa. The difference between the experimental and published data can be justified based on the reasons given in Section 6.1 and further reasons will be presented below.

First considering the Hugoniot developed by the experimental data compared to Nagayamas Hugoniot which are shown in Equation 35 and Equation 36.

$$U_s = 0.1022U_p + 1681 \quad (35)$$

$$U_s = 1.99U_p + 1453 \quad (36)$$

Nagayamas data has a larger slope and sound speed with the values being 1.99 and 1453 m/s. Paul Cooper's, *Explosive Engineering*, has a slope and sound speed of 1.921 and 1647 m/s. Comparing Nagayama with the experimental data to Paul Coopers results shows an interesting take on the data. The bulk sound speed of Coopers book is comparable to the experimental data with only a 2% difference. The percent difference associated the Nagayama's bulk sound speed when compared to the accepted value of Cooper's is around 12%. However, when comparing the slope of the line, Cooper and Nagayama's data is within range with just about 4% difference compared to the experimental data which has a difference around 94%. There are many possible explanations for the lack of a slope in the Hugoniot determined by the experimental data.

A possible source of the differences between the published data and the experimental data could have resulted from the water that was used. Authors such as Cook and Mori used distilled water that was boiled prior to experimenting [15] [2].

Sharipdzhanov used distilled water that filtered from an ice bath into the sample continuously while experimenting [17]. The water that was used in the experiment was obtained from a drinking fountain with a filter at Engineering Hall. The water is surface water from Milwaukee's Water Works [32]. Even with the filter by Milwaukee and in the drinking fountain, the water still contains minerals. The water contained a high amount of aluminum and copper at 3 8.93 ppb and 406.1 ppb [33]. The excess metal in the water could cause the shock front to have a different travel path than distilled water. The second difference in the water that was used compared to published data was the lack of boiling the water prior to testing. Unboiled water can contain air bubbles that can cling to the walls during an experiment obstructing the wave front [4]. However, it is hard to compare both sets of data considering one water sample is pure and the other has different minerals.

On the similar issues of water's compressibility is its density. As pressure increases in the water sample during the experiment, the density of the water can also increase from shock compression. To find the experimental results, the water's density was assumed constant throughout the calculations at 998 g/m^3 [22]. However, the actual density of the specimen could have been higher or lower and as the experiment progresses, the density changes due to the local variations in temperature and pressure. However, this is a minor uncertainty and was taken into consideration while doing Taylor Series Error Analysis [30].

6.3 Analysis

While the results are different from other published data, this is one of the first experiments conducted at atmospheric pressures with tap water. Using tap water in the experiment has many benefits when compared to using distilled and boiled water. First, it is more practical for field applications. The Department of Defense has interest in water studies and rarely when performing field jobs will they involve distilled water. In regards to the medical field, the shock impedance of water is similar to that of living tissues [4]. Living beings do not consume distilled water so the water used in this study would be beneficial for living tissue analysis. The lower pressures is also beneficial for the medical field as living tissues can be damaged at high pressures.

While the experimental results are different then the published data, it can still be assumed the experimental process has some validity. The simulated results of the experiment are near the published data. The goal of the simulations was to find the change in time from when the wave reached the front to the back surface of a given thickness of water. After determining the change in time, the same impedance matching techniques and calculations were performed on the data. Also, to find the simulations, the same flyer velocities and target dimensions were used. The only difference between the simulations and experimental results then is the change in time. This leads one to believe the main error in the variation in the results come from the PZT false triggering during the experiment and causing an increase in the experimental time. A shorter change in time would have caused an increased shock velocity and that would have resembled more closely to the published data.

Even with a larger shock velocity, the results would still have a small slope because of the low shock pressure that was achieved. The shock pressure is a function of flyer velocity, particle velocity, density, slope, and the bulk sound speed. Increasing any of these variables would result in a higher shock pressure. It is also possible to perform the experiment in a vacuum which would allow for an increase in pressure.

7. Conclusion

7.1 Future work

The experiment is important to the defense industry and the medical field. The medical field is in need of more accurate experimental results that agree with theoretical results prior to testing on living tissues. There are numerous opportunities for this analysis to be continued and improved.

Firstly, the experimental process can be improved to provide more accurate results. A larger and improved dual diaphragm light gas gun with a 2" barrel is currently being designed and built at Marquette University. The dual diaphragm gas gun can be pulled to a vacuum and can reach flyer velocities up to 1500 m/s. If the experiment were to be conducted on the larger gas gun, there would be less limitations on the size and design of the target. Rather than the design having a PZT pin in the water, a Mangyan pressure gage could be placed on the front surface of the water to get the arrival time of the shock wave. A PDV would still be used to find the arrival on the back surface of the water. The larger barrel would allow the ratio between the water thickness and flyer size to be increased. With a thicker sample of water, a thin reflective strip could be placed in the water with a minimal volume offset. If the thin reflective surface is in the center of the water sample, a PDV collimator could be used to determine when the wave reaches the center of the sample. This would help characterize the shock structure of water. In previous studies, the end states of the shock structure are connected and with the addition of the thin reflective tape, the middle state could be characterized. With the new

experimental set up, it would be interesting to analyze the experiment using tap, distilled, and boiled water.

In addition to changing the experimental apparatus, more calculations could be performed to further characterize the water under shock. For example, the shock temperature along a Hugoniot can be calculated. However, the shock temperature is based on the thermodynamic constants along the Hugoniot so the Hugoniot must be extremely accurate. Once pressure, volume and temperature are known, most thermodynamic properties can be determined from those relations. This includes mechanical and thermodynamic work which could describe the dynamic strength of the material under shock.

7.2 Conclusions

An experiment was conducted at Marquette University in the Shock Physics Laboratory. The goal of the experiment was to experimentally characterize the shock structure of water. This experiment differs from previously published experiments in that it achieved lower than normal shock pressures with an average of 0.47 GPa and the water sample was tap water rather than distilled water. To conduct the experiment, a single stage 12.7 mm gas gun was used to fire a projectile into a stationary target filled with water. The projectile was made of copper, PMMA, or aluminum and ranged in velocities from 200 to 350 m/s. The water was obtained from Engineering Hall at Marquette University and was tap water. To acquire data, three oscilloscopes were connected to graphite break pins, a Piezoelectric Pin and a Photo Doppler Velocimeter. MATLAB and

Maple Soft were used to calculate the shock velocity and particle velocity of the water sample.

The experimental results were calculated at pressures below 1 GPa. The results were compared to simulated results and published data. The Hydrocode called CTH was developed by Sandia National Laboratories [5]. After plotting the experimental and simulated results, a Hugoniot line was fitted to the data to characterize the water's bulk sound speed and slope. The experimental results differed from the simulated and published results. It is believed that a false trigger from the PZT pin is the cause in the differences between the simulated and experimental results.

The scientific community is interested in furthering the understanding of shock wave structure of water, given its implications in a wide range of applications; from researching how shock waves penetrate unwanted body tissues to studying how humans respond to blast effects. There is interest in the health field, defense industry, and planetary sciences to understand the effects of shocking water. Shock waves have even been used to purify water containing copper, boron, and lead [3]. The study of shock waves in water is important as the properties of water are close to that of living tissues which helps in the medical and defense industry [2].

If future experiments were to take place, the new and improved dual diaphragm light gas gun with a 2" barrel at Marquette University would be utilized. This would allow the target to be larger and more measurement devices could be placed on the water sample. With a larger sample, the middle state of the water could be determined if a thin reflective strip of material is in the middle of the sample's thickness. This would allow the Hugoniot to be determined from beginning, middle and end states.

BIBLIOGRAPHY

- [1] G. Ben-Dor, O. Igra and T. Elperin, *Handbook of Shock Waves*, London: Academic Press, 2001.
- [2] Y. Mori, "New Water Shock Sensor," *Review of Scientific Instruments*, vol. 72, no. 4, pp. 2123-2127, 2001.
- [3] Putman Media Incorporated , "Shockwave Purifies Water," *Chemical Processing* , 2016.
- [4] K. Nagayama, "Shock Hugoniot compression curve for water up to 1 GPa by using a compressed gas gun," *Journal of Applied Physics* , vol. 91, no. 1, pp. 476-482, 2002.
- [5] J. M. McGlaum, S. L. Thompson and M. G. Erlick, "Int. J. Impact.," *Eng. 10*, pp. 351-360, 1990.
- [6] K. Nagayama, Y. Mori, K. Shimada and M. Nakahara, "Shock hugoniot compression curve for water up to 1 GPa by using a compresses gas gun," *Journal of Applied Physics*, vol. 91, no. 1, pp. 476-482, 2002.
- [7] "Follow the Water," NASA, [Online]. Available: NASA.gov.
- [8] D. X. Hammer, G. Noojin, T. Robert , C. Clary, B. Rockwell and C. Toth, "Intraocular laser surgical prove for membrane disruption by laser-induced breakdown," *Applied Optics*, vol. 36, no. 7.
- [9] M. Theil, "Application of schock waves in medicine," *PubMed*, pp. 18-21, 2001.
- [10] K. Teshima, T. Ohshima, S. Tanaka and T. Nagai, "Biomechancial effects of wave on Escherichia coli and phage DNA," *Shock Waves*, no. 293-297, 1995.
- [11] C. E. Ragan, M. G. Silbert and B. C. Diven, "Shock Compression of Molybenum to 2.0 TPa by Means of a Nuclear Explosion," *Journal of Applied Physics* , vol. 48, 1977.
- [12] G. A. Lyzenga and T. J. Ahrens, "The temperature of shock-compressed water," *The Journal of Chemical Physics*, vol. 76, no. 12, 1998.
- [13] S. T. Stewart and T. J. Ahrens, "Shock Hugoniot of H₂O Ice," *Geophysical Research Letters*, vol. 30, no. 6, 2003.
- [14] S. Stewart, "Shock Properties of H₂O Ice," *Journal of Geophysical Research* , vol. 10, 2005.

- [15] M. A. Cook , R. T. Keyes and W. O. Ursenbach, "Measuremnts of Detonation Pressure," *Journal of Applied Physics* , vol. 33, no. 12, pp. 3413-3421, 1962.
- [16] P. Lynse, "A Comparison of Calculated and Measured Low-Stress Hugoniots and Release Adiabats of Dry and Water-Saturated Tuff," *Journal of Geophysical Research*, vol. 75, no. 23, pp. 4375-4386, 1970.
- [17] I. Sharipdzhanov, "Anomalies in the Shock and Isentropic Compressibilities of Water," *Fizika Goreniya i Vzyva*, vol. 19, no. 5, pp. 149-153, 1983.
- [18] L. Al'tshuler, "Dokl. Akad. Nauk SSSR," vol. 1, no. 67, 1958.
- [19] J. Smityh, "The Hydrogen Bond and the Water Molecule".
- [20] NASA, "Global Maps," July 2002. [Online]. Available: http://earthobservatory.nasa.gov/GlobalMaps/view.php?d1=MYDAL2_M_SKY_WV. [Accessed November 2016].
- [21] R. B. Bird, W. E. Steart and E. N. Lightfoot, "Diffusivity and the Mechanisms of Transport," in *Transport Phenomena* , John Wiley & Sons, Inc. , 2007, pp. 514-515.
- [22] P. W. Cooper, Explosives Engineering, Wiley-VCH, Inc. , 1996.
- [23] Oxford Dictionaries , "English Oxford Living Dictionaries," Oxford University Press , [Online]. Available: en.oxforddictionaries.com.
- [24] "New World Encyclopedia," 15 September 2015. [Online]. Available: www.newworldencyclopedia.org. [Accessed December 2016].
- [25] G. Elert, "The Physics Hypertextbook," [Online]. Available: <http://physics.info/shock/>. [Accessed August 2016].
- [26] "Mini Plasma Sputtering Coater with Vacuum Pump & Gold Target, 1.5" Max Sample - GSL-1100X-SPC12-LD," MTI Corporation , [Online]. Available: <http://www.mtixtl.com> [Accessed January 2017].
- [27] "McGlaum, J.M., Thompson, S.L., and Erlick, M.G., Int. J. Impact. Eng. 10, 351-360, 1990," [Online].
- [28] "CA-1136," Dynasen, Inc. , [Online]. Available: <http://dynasen.com/product/ca-1136/>. [Accessed 31 January 2017].
- [29] E. Weisstein, "Fast Fourier Transform," Wolfram MathWorld , [Online]. Available: <http://mathworld.wolfram.com/FastFourierTransform.html>.

- [30] J. Borg, *Error Analysis Laboratory Uncertainty in Measured Quantity*, Milwaukee Wisconsin.
- [31] S. D. Hamann and M. Linton, "Electrical Conductivities of Aqueous Solutions of KCl, KOH, and HCl, and the ionization of Water at High Shock Pressures," *Division of Applied Chemistry*, vol. 2196, pp. 2186-, 1969.
- [32] "Milwaukee Water Works," [Online]. Available: milwaukee.gov.
- [33] M. Dollhopf, *Engineering Hall Water Report*, Milwaukee: Water Quality Center.
- [34] "Science Learning Hub," Sci, [Online]. Available: <http://sciencelearn.org.nz/Contexts/Light-and-Sight/Science-Ideas-and-Concepts/Refraction-of-light>. [Accessed December 2016].
- [36] Quorum Technologies, "Sputter Coating Technical Report," Kent, 2002.

8. Appedix

8.1 Experimental Error

The early stages of testing and design had multiple errors which will be described below in detail. The initial design of the experiment was a big source of error in the first shot fired at Marquette University. The design featured two PDV collimators reflecting off of gold speckle coating located at the front and back surface of the water. Shown in Figure 75 , is the target mounted to the target plate with two collimators exiting the target.



Figure 75: Original target sample with two PDV collimators exiting the design mounted onto the target plate.

The first experimental error in the above figure was derived from neglecting to acknowledge that light refracts in water. The PMMA and water have different refractive indexes which causes the light to bend once it enters the water [34]. When the light bent in the sample, there was no light return from the front surface of the water. The goal of

the collimators was to determine the time of arrival of the shock wave on the front and back surface of the water. Without proper light return, the time of arrival of the shock wave could not be determined. To combat this problem, a PZT pin was added to the design before shooting. Since the collimators were glued into the target, a drill press was used to create a hole for the PZT pin to fit through. The PZT pin was placed into the target and glued from the back side so the pin touched the front surface of the water. With this addition, a third oscilloscope was needed to trigger off of the impact of the flyer which signaled the beginning of the shock wave at the front surface of the water. Shown in Figure 76 , is the modified target design with the original collimators and the PZT pin.

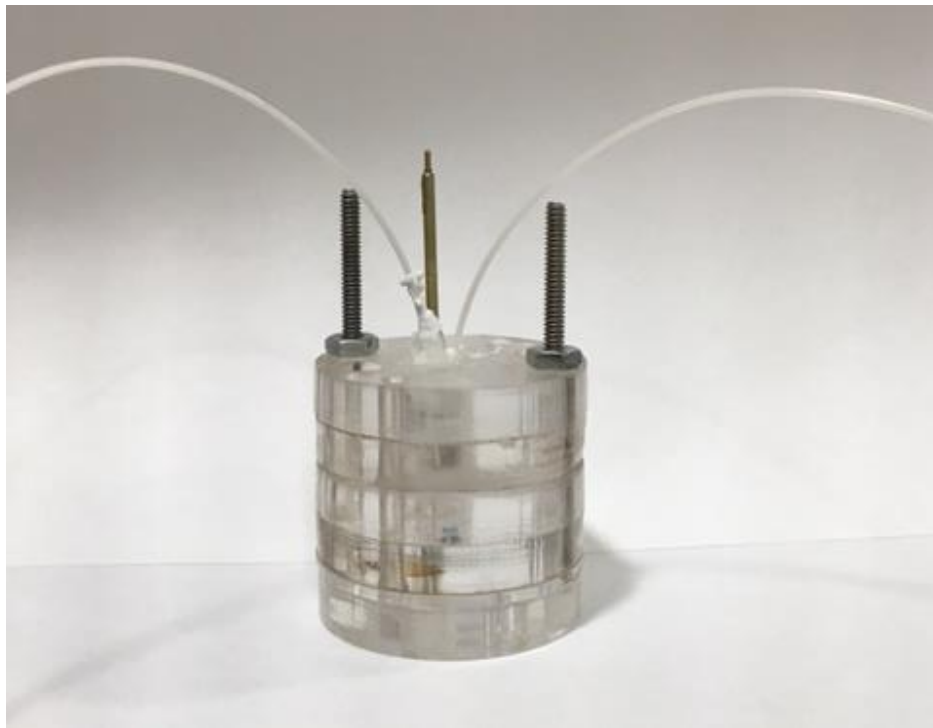


Figure 76: Modified target design for shot one.

During the experiment, the PZT pin acquired a signal but the PDV collimators did not. This was caused from there being poor light return from the back surface of the water. When aligning the collimators to the target, there was good light return from the

back surface but after moving the target and using a drill press on the target, the collimator shifted in position and was no longer aligned. While the collimator was glued in place, the channel of the target it was held in had too large of diameter so it would have been easy for the collimator to shift. The collimators are extremely sensitive to location and alignment and this was unknown before conducting the first experiment.

The second shot involved similar error as before in regards to the collimators. The target was redesigned to feature one collimator and one PZT pin. Figure 77 shows the target with one PZT pin and one collimator.

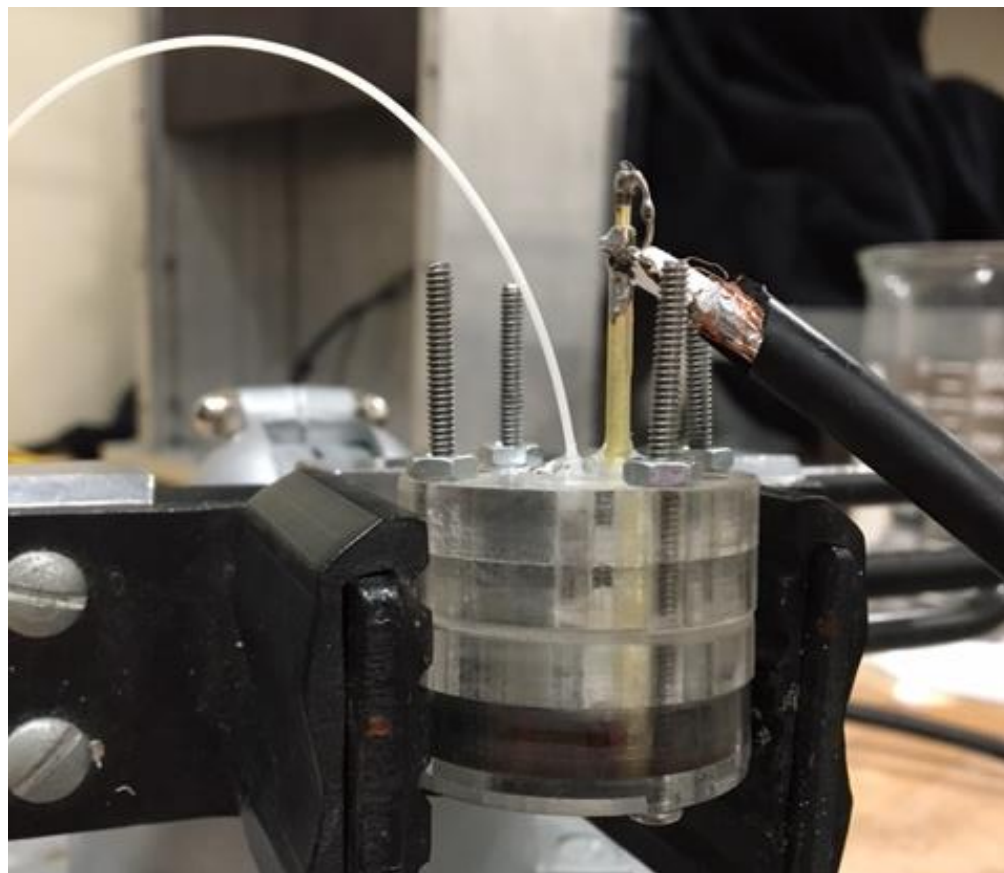


Figure 77: Target for the second shot featuring one collimator and one PZT pin.

To begin, the diameter that the collimator was placed in a guide channel that was still slightly too large and even after super gluing the collimator in place once aligned, there was still room for movement. While mounting the target or while filling the water, the collimator shifted and the light return from the PDV was lost. Thus, there was not data from the back surface of the water to know when the shock arrived.

When assigning the settings to the PZT pins oscilloscope, the sampling rate was not considered. Because of this, the oscilloscope triggered when the pin signaled 500 mV however it did not collect data. This was due to the sampling rate being too low so the scope skipped over the useful data in the system. For the next shot, the scope was set to sample at 2.5 GSa/s which allowed 10K points to be collected. This led to a successful shot and the first file of useful data that calculations were done on.

Prior to mounting the target for the first and second shot, the water had to be filled. To fill the water, the four screws were slightly loosened and the four back plates were held together and lifted away from the two front plates. A micropipette injected water into the housing and the plates were pushed back together. Using the force from a hand to hold the plates together the screws were tightened quickly to eliminate the loss of water from its housing. This process is necessary but should have been completed prior to aligning the PDV collimators. Even though the three back plates were held together, they could have shifted apart and caused the collimators to also shift. To combat this issue prior to the third shot, the back plates of the target were first super glued together with Loctite Super Glue so they could not come apart. Next, prior to aligning the collimators in the target, the target was filled with water and mounted onto the target plate. The collimators were aligned while the target was mounted and then glued in place with

Loctite Super Glue. The glue was allowed to set for 30 minutes and then the shot was fired.